The heterogeneity of dermal mesenchymal cells reproduced in skin equivalents regulate barrier function and elasticity.

Shun Kimura[1*], Sachiko Sekiya[2, 3], Sawa Yamashiro[1], Tetsutaro Kikuchi[2], Masatoshi Haga[1], & Tatsuya Shimizu[2]

[1] *ROHTO Pharmaceutical Co., Ltd., Osaka, 544-8666, Japan*

[2] *Institute of Advanced Biomedical Engineering and Science, TWIns, Tokyo Women's Medical University, Tokyo, Japan*

[3] *Institute of Integrated Research Human Biology Research Unit, Institute of Science Tokyo, Tokyo, Japan*

*Correspondence to: skimura@rohto.co.jp

Manuscript information:

This manuscript comprises 63 pages of text, 5 figures, and 1 table.

Abstract

The heterogeneity of dermal mesenchymal cells, including perivascular mesenchymal cells and papillary and reticular fibroblasts, plays critical roles in skin homeostasis. Here, we present human skin equivalents (HSEs) in which pericytes, papillary fibroblasts, and reticular fibroblasts are spatially organized through autonomous three-cell interactions among epidermal keratinocytes, dermal fibroblasts, and vascular endothelial cells. The replication of dermal mesenchymal cell heterogeneity enhances skin functions, including epithelialization, epidermal barrier formation, and dermal elasticity, enabling the *in vitro* evaluation of drug efficacy using methodologies identical to those used in human clinical studies. Furthermore, we found that ascorbic acid-induced epidermal turnover and well-aligned extracellular matrix synthesis via perivascular niche cells play crucial roles in improving skin aging phenotypes. HSEs with heterogeneous dermal mesenchymal cells will improve our understanding of the mechanisms underlying skin homeostasis through cell-to-cell communication and serve as an alternative model to animal experiments for the development of precision medicine.

36 **Introduction**

37 The integumentary organ system (IOS), which includes the skin, skin
38 appendages, nerves, and blood vessels, plays essential roles in waterproofing, cushioning,
39 protecting deeper tissues, excreting waste and thermoregulating[1]. The dermis,
40 characterized by appropriate stiffness and elasticity, is anatomically divided into two
41 distinct layers: the upper layer, called the papillary dermis, which is located directly
42 beneath the epidermis and is composed of thin and poorly oriented collagen fibers, and
43 the lower layer, called the reticular dermis, which is adjacent to the subcutaneous layer
44 and consists of thick and directionally oriented collagen fibers[2,3]. Skin
45 microcirculation is organized into two horizontal plexuses: one located at the
46 boundary between the papillary and reticular dermises and the other situated
47 at the interface between the reticular dermis and the subcutaneous layer[4].
48 The alignment of collagen fibers, skin appendages such as hair follicles, and
49 the vascular system within the dermis conforms to the direction of intrinsic
50 tensile force vectors known as tensional homeostasis, enabling the skin to
51 function effectively as a cushion with optimal strength[5]. The dermal
52 mesenchymal cells distributed within the dermis include not only papillary
53 and reticular fibroblasts but also various subpopulations, such as dermal

54 papilla cells, arrector pili muscle cells, mesenchymal stem cells, and
55 pericytes[6,7]. Dermal fibroblasts not only synthesize extracellular matrix (ECM)
56 components such as collagen and elastin to regulate the flexibility and physical properties
57 of the dermis but also contribute to the structural and functional homeostasis of the IOS
58 through crosstalk with adjacent tissues such as the epidermis, hair follicles, and blood
59 vessels. This crosstalk is achieved through cell-to-cell communication mechanisms,
60 including the secretion of growth factors such as KGF, TGF-β, and VEGF and cell
61 adhesion signaling via integrins and laminins[8–10]. Analysis of cell surface marker
62 expression and single-cell RNA sequencing (scRNA-seq) have progressively elucidated
63 distinct fibroblast lineages and their functional characteristics, defined by the expression
64 patterns of specific genes such as CD90, CD39, CD36, SFRP2, FMO1, and FAP[11,12].
65 Importantly, these fibroblast lineages are influenced by factors such as age, anatomical
66 location, and endogenous and exogenous stresses, resulting in changes that affect
67 physiological processes, including wound healing, fibrosis, atopic dermatitis, and
68 aging[13–16]. Consequently, they are considered promising mechanistic targets for next-
69 generation precision medicine and health care products[17].

70 Age-related declines in the epidermal barrier and cushioning functions lead not
71 only to medical issues such as senile xerosis and skin tears but also to aesthetic concerns

72 such as dryness, disrupted skin texture patterns, wrinkles, and sagging, all of which
73 diminish quality of life[18]. A reduction in proliferative Ki67-positive basal epidermal cells
74 with age leads to decreased turnover, resulting in epidermal thinning[19]. The epidermal
75 barrier function either remains unchanged or declines with age depending on the area,
76 increasing the risk of pruritus and dermatitis[18,20,21]. In aged skin, the papillary dermis is
77 relatively thinner, and the epidermal rete pegs and dermal rete ridges are shorter, resulting
78 in a flattened epidermal-dermal junction. This morphological change reduces epidermal
79 resistance to shearing forces and thereby makes the epidermis more fragile[22]. Additionally,
80 collagen fibers and elastic fibers, which constitute the basement membrane and dermal
81 layer, undergo fragmentation and reduction due to MMPs and elastase, leading to a
82 decrease in skin elasticity[23]. Simultaneously with the degradation of dermal collagen, the
83 extracellular matrix (ECM) of the vascular wall diminishes, leading to vascular atrophy,
84 reduction, and disruption of orientation[24]. This process is thought to destabilize not only
85 the nutritional supply to the skin but also the resistance to tensile loading[25,26]. *In vitro*
86 analyses of anatomically isolated papillary and reticular fibroblasts have revealed that,
87 compared with reticular fibroblasts, papillary fibroblasts exhibit high cell proliferative
88 activity and promote epithelialization through KGF production. Notably, these
89 characteristics are lost with aging or cellular senescence induced by serial passaging[27,28].

90 Moreover, recent scRNA-seq analyses of sun-protected human skin have shown that
91 specific spatial and functional transcriptomic characteristics exhibited by dermal
92 fibroblast subpopulations are lost with age, supporting the findings of *in vitro* studies[13].
93 Perivascular cells are also known for their active synthesis of ECM components,
94 including collagen and laminin, as well as their role in promoting epithelialization during
95 skin regeneration. The decline in perivascular cells associated with vascular aging is
96 suggested to be a potential contributor to skin aging[29]. Interestingly, aging-related changes
97 in dermal fibroblasts are highly sensitive to systemic metabolic shifts, and long-term
98 caloric restriction can reversibly prevent the senescence-associated phenotypic
99 transformation of dermal fibroblasts. In summary, the loss of cellular identity is a
100 fundamental mechanism underlying organ aging, and the development of therapeutic
101 strategies to delay aging through dietary and metabolic interventions holds great
102 promise[30,31].

103 Experimental models using animals with a short lifespan that allow for genetic
104 modification, cellular lineage tracing, and histological analysis have greatly contributed
105 to elucidating the mechanisms of aging. However, animal experimentation not only
106 requires careful consideration of interspecies differences with humans but also faces
107 increasing societal demands for a reduction in animal clinical studies[32–35]. Human cell-

108 based *in vitro* research models such as primary cultured cells, organoids, and artificial
109 tissues are being explored as preclinical research tools to replace animal
110 experimentation[36]. Primary cultured cells are fundamental tools for studying skin aging
111 and related diseases; however, the culture process significantly impairs the gene
112 expression profiles and differentiation potential of dermal mesenchymal cells such as
113 papillary fibroblasts, dermal papillae, and pericytes[12,29]. Organoids that replicate not only
114 the integumentary organ system itself, including appendages such as hair follicles, but
115 also its cellular heterogeneity are anticipated to advance the understanding of cell-cell
116 interactions within the microenvironment and to be applied in drug discovery screening
117 systems[37,38]. However, organoids are difficult to enlarge because of their oxygen
118 requirements and other reasons, making them unsuitable for tissue-scale evaluations of
119 functions such as the skin's barrier function and elasticity[39,40]. Human skin equivalents
120 (HSEs) can partially reproduce physiological skin functions such as its barrier function,
121 proliferative capacity, ECM synthesis, cellular signaling and responses to various stimuli,
122 and are utilized worldwide as alternative animal models for evaluating the efficacy and
123 safety of commercially available formulations essential for sustainable research and
124 development[41,42]. HSEs constructed using distinct dermal mesenchymal cell
125 subpopulations, such as fibroblasts, pericytes, and senescent cells, are ideal models for

126 visualizing the impact of cell-to-cell communication between target cells for research on
127 skin tissue organization[12,27,29]. Furthermore, HSEs enable the reproduction of
128 mechanobiological environments. We previously demonstrated that tissue-scale tensional
129 homeostasis regulates skin's structural and physiological functions, such as
130 epithelialization and ECM production, via myocardin-related transcription factor A
131 (MRTF-A) activation[43]. Based on the growing evidence linking dermal mesenchymal cell
132 heterogeneity and aging, generating *in vitro* research models that replicate skin's cellular
133 heterogeneity and allow for functional evaluation is essential for the development of
134 therapies to counteract the effects of skin aging[31].

135 In this study, we developed an HSE that replicates the heterogeneity of human
136 dermal mesenchymal cells, including pericytes, papillary fibroblasts, and reticular
137 fibroblasts, by utilizing commercially available primary cells, specifically normal human
138 epidermal keratinocytes (NHEKs), normal human dermal fibroblasts (NHDFs), and
139 human umbilical vein endothelial cells (HUVECs). We found that the cell-to-cell
140 communication among these three types of cells within a collagen- and fibrin-based three-
141 dimensional environment plays a crucial role in promoting epithelialization, dermal ECM
142 deposition, and the formation and stabilization of vascular structures by reproducing
143 dermal mesenchymal cell heterogeneity *in vitro*. Our HSEs replicated an aging skin

144 phenotype, including epidermal barrier disruption and reduced skin elasticity, in a 12-d
145 long-term culture in nutrient-poor medium, leading to epidermal thinning, an imbalance
146 in collagen synthesis and degradation, and a loss of vascular structural alignment. The
147 ability of ascorbic acid to mitigate these impairments in skin function was clearly
148 demonstrated via a human clinical trial protocol. This study provides an *in vitro*
149 evaluation platform that will contribute to the sustainable advancement of the health care
150 industry.

151 **Results**

152

153 **Tricellular communication among epidermal keratinocytes, dermal fibroblasts,**

154 **and vascular endothelial cells enhances the organization of skin and blood vessels.**

155 In the development and regeneration of different organs, cell-to-cell

156 communication plays an essential role in inducing and maintaining the differentiation of

157 constituent cells[35]. Recent findings suggest that a specific subset of tissue-resident

158 mesenchymal cells located close to blood vessels plays a key role in epidermal

159 differentiation and ECM production[6,44,45]. Therefore, we hypothesized that by

160 vascularizing an HSE and reproducing cell-to-cell communication on the basis of the

161 reconstructed perivascular niche, it would be possible to construct an HSE that more

162 faithfully replicates the *in vivo* characteristics of skin.

163 To investigate the role of communication among epidermal keratinocytes,

164 dermal fibroblasts, and vascular endothelial cells in skin tissue formation, we

165 reconstructed HSEs each incorporating one to three types of these constituent cells (Fig.

166 1a, b). All HSEs were constructed via the method we previously reported for

167 reproducing tensional homeostasis in a skin model[43]. After 14 d of air lift culture, the

168 reconstructed tissue was 12 mm in diameter and 1-2 mm in thickness. The E and EV

169 models were transparent and extremely soft (Fig. 1b). HE staining was used to visualize
170 the regulation of skin and blood vessel organization through cell-to-cell communication
171 (Fig. 1c). In the E and EV models, an abnormal epidermis lacking a basal cell layer
172 formed, whereas normal epithelialization was observed in the ED and EDV models. This
173 finding indicates that crosstalk between NHEKs and NHDFs is essential for
174 epithelialization. Endothelial tubes in the dermis were observed only sparsely in the V
175 and EV models but were distributed throughout the skin in the DV and EDV models. In
176 particular, the endothelial tubes in the EDV model tended to orient
177 horizontally along the skin surface and increased in number with increasing
178 distance from the epidermis. Sirius red staining revealed localized collagen
179 fiber deposition (Fig. 1d). In the ED model, collagen fiber formation was
180 confirmed at the epidermal-dermal junction, because of the well-known
181 interaction between the epidermis and dermis. In the DV and EDV models,
182 the collagen deposition distribution within the dermis was similar to that of
183 the endothelial tubes. Interestingly, collagen deposition at the epidermal-
184 dermal junction and around endothelial tubes appeared to be promoted in
185 the EDV model compared with the ED and DV models.
186 The morphogenesis of the epidermis, endothelial tube, and dermis in

187 each HSE was analyzed via immunohistological analysis. The results of
188 epidermal marker staining demonstrated that the epidermis of the ED and
189 EDV models exhibited a CK5-positive basal layer, a CLDN1-positive basal
190 to granular layer, FLG-positive keratohyalin granules, and a CK10-positive
191 stratum corneum, closely resembling the epidermis of natural human skin
192 (Fig. 2a). Furthermore, the number of Ki67-positive cells was greatest in the
193 EDV model and lower in the ED, EV, and E models (Fig. 2b). The trans-
194 epidermal water loss (TEWL) in the EDV model was 9.68 g/m^2h, and water
195 evaporation was significantly suppressed compared with that in the ED model (Fig. 2c).
196 These results indicate that dermal fibroblast-epidermal keratinocyte
197 communication, which promotes epithelialization and barrier function, is
198 enhanced by vascular endothelial cells.

199 Immunostaining for the endothelial cell markers CD31 and vWF
200 revealed active endothelial tube formation in the presence of both HUVECs
201 and NHDFs (Fig. 2d). In the DV and EDV models, the deposition of collagen
202 types 1 and 4 was observed around the endothelial tubes, suggesting that
203 fibroblast-endothelial cell crosstalk stabilizes the endothelial tube structure
204 through ECM synthesis (Fig. 2d). In the ED model, type 1 collagen fiber

205 formation in the dermis was stimulated around the epidermal-dermal
206 junction, whereas in the EDV model, additional strong type 1 collagen
207 expression originating from endothelial tubes was observed, resulting in the
208 formation of collagen fibers that spread throughout the entire dermis. In
209 addition, 3/4-length fragmented type 1 collagen, a product of MMP-8-
210 dependent type 1 collagen fiber digestion, was detected exclusively in the
211 dermal ECM of the E and EV models, indicating that keratinocyte-fibroblast
212 interactions control the balance between collagen fiber synthesis and
213 degradation (Fig. 2d). Natural human skin microcirculation is organized into
214 horizontal plexuses situated 1-1.5 mm below the skin's surface[4].
215 Immunostaining for CD31 and type 1 collagen revealed that the blood
216 vessels and collagen fiber in the EDV model were distributed in parallel to
217 the epidermal plane, and mathematical assessment via two-dimensional fast
218 Fourier transform (2D-FFT) analysis corroborated this observation (Fig. 2e).
219 The collagen network, which is arranged parallel to the skin surface,
220 functions to withstand mechanical forces acting perpendicular to the skin.
221 Therefore, we evaluated the elasticity of HSEs, a physical indicator of skin
222 aging and a correlating factor of wrinkles and sagging, using the Cutometer-

223 based protocol applied in human clinical studies. [46]. Skin elasticity could be
224 measured only in the ED and EDV models because the tissue in the other HSEs was
225 damaged by negative pressure loading. The ED and EDV models withstood 10 negative
226 pressure loading cycles (Fig. 2f). The R7 value, which is an elasticity index that is
227 reportedly associated with facial sagging, increased in the EDV model (Fig. 2g).

228 In conclusion, we have demonstrated that tricellular interactions
229 among epidermal keratinocytes, dermal fibroblasts, and endothelial cells
230 play critical roles in epidermal turnover, collagen synthesis, and
231 angiogenesis and are sufficient to enhance tissue-scale skin functionality,
232 including viscoelastic properties and the integrity of the epidermal barrier.

233

234 **Cell-to-cell communication in a three-dimensional environment replicates dermal**
235 **mesenchymal cell heterogeneity that is lost in two-dimensional culture.**

236 To evaluate the impact of vascularization on fibroblast heterogeneity in the HSEs,
237 we observed the spatial distribution of cells with positive markers for papillary fibroblasts
238 (CD39 and FAP), reticular fibroblasts (CD36 and CD90), and pericytes (NG2 and αSMA)
239 via immunohistochemical analysis (Fig. 3a and Supplementary Fig. 1). Fibroblasts in
240 the D model were positive for the pan-fibroblast marker vimentin, but the

241 expression of all the markers in papillary and reticular fibroblasts and
242 pericytes was barely detectable. CD39-positive cells were observed in the DV
243 and EDV models, and FAP-positive cells were observed in the ED and EDV
244 models. Interestingly, CD39-positive cells tended to localize around the
245 endothelial tubes, whereas FAP-positive cells were observed mainly near the
246 epidermal-dermal junction; similar patterns were also observed in natural
247 human skin. CD36-positive cells were distributed in the DV and EDV models,
248 and CD90-positive cells were widely distributed in the DV, ED, and EDV
249 models. NG2- and αSMA-positive pericytes were localized to the periphery of
250 the lumen formed by vWF-positive vascular endothelial cells.

251 Immunohistochemical analysis revealed that the fibroblasts
252 constituting the HSEs exhibited heterogeneity in terms of cell surface marker
253 expression, depending on the cell types included in the model. Therefore, we
254 conducted scRNA-seq to analyze the single-cell transcriptomes of dermal
255 mesenchymal cell populations within the HSEs. We profiled three samples:
256 the ED and EDV models cultured at the air-liquid interface for 14 d, as well
257 as a mixture of NHEKs, NHDFs, and HUVECs cultured separately under
258 two-dimensional conditions (referred to as 2D) (Fig. 3b). In an initial analysis,

259 we obtained an overview of the diverse cell populations by integrating the
260 cells from three samples. After quality filtering, a total of 23,911 cell profiles
261 were successfully obtained across all conditions. A uniform manifold
262 approximation and projection (UMAP) plot revealed three major cell
263 populations and 20 distinct clusters (Fig. 3c-left). Based on the existing
264 marker genes, we identified the four cell types (keratinocytes, fibroblasts,
265 vascular ECs, and pericytes) for each cell culture (Fig. 3c-right). The UMAP
266 plot illustrates the specific impact of each culture condition on the fibroblast
267 population (Supplementary Fig. 2a). The major fibroblast clusters under 2D,
268 #1, #6, #13, and #17, were relatively minor subpopulations in the ED and
269 EDV models. #0, #2, #9, #10, and #11 were major clusters in both the ED and
270 EDV models, but cluster #14, characterized by the expression of pericyte
271 marker genes (*ACTA2* and *RGS5*), was detected as a subpopulation unique to
272 the EDV model (Fig. 3d). We hypothesized that the formation and
273 maintenance of cluster #14 involves endothelial cell-fibroblast
274 communication and investigated this interaction via CellChat analysis[47].
275 Compared with cluster #9, cluster #14 showed increased signaling through
276 VEGFB-VEGFR1, PGF-VEGFR1, laminin-dystroglycan, and laminin-

277 integrin interactions (Fig. 3e). Compared with the 2D conditions, the ED and
278 EDV models promoted the expression of collagen fiber-related genes such as
279 *COL1A1*, *COL3A1*, *COL4A1*, *COL4A2*, and *COL5A3* but suppressed the
280 expression of elastic fiber-related genes, including *ELN* and *FBN1* (Fig. 3f).
281 This transcriptome change was more pronounced in the EDV model,
282 suggesting the contribution of cluster #14.

283 To investigate the biological significance of the HSEs' dermal
284 mesenchymal cell heterogeneity, we referred to a published *in vivo* human
285 skin scRNA-seq dataset from L Solé-Boldo *et al.* and integrated it with our
286 HSE datasets via the R Harmony data integration algorithm[13]. A UMAP plot
287 revealed four major cell populations and 11 distinct clusters (Fig. 4a). To
288 distinguish the results of this integrated analysis from those of the previous
289 *in vitro* data analysis, apostrophes were added to the cluster numbers
290 indicated in this analysis. The four major clusters were defined as
291 keratinocytes, fibroblasts, vascular endothelial cells, and pericytes according
292 to the expression patterns of marker genes (Fig. 4b). In the ED and EDV
293 models, similar to *in vivo* skin, fibroblasts were composed of mainly clusters
294 #0', #1', and #8'. In contrast, 2D-cultured fibroblasts contained very few cells

295 from clusters #0' and #8', whereas clusters #2' and #11', which are rarely found
296 in natural human skin, comprised their main subpopulations (Fig. 4c). Cell
297 cycle scoring via the Seurat scRNA-seq analysis pipeline (ccSeurat)[48]
298 (https://satijalab.org/seurat/v3.1/cell_cycle_vignette.html) revealed that cells
299 in cluster #2', characteristic of 2D-cultured fibroblasts, were in the G2/M and
300 S phases (Fig. 4d). L Solé-Boldo *et al.* defined four main fibroblast
301 subpopulations that could be spatially localized and showed differential
302 secretory, mesenchymal and proinflammatory functional annotations. We
303 reanalyzed this dataset to identify these four fibroblast subtypes as well as
304 pericytes (Supplementary Fig. 3). We then plotted the cells corresponding to
305 each subtype on the integrated UMAP plot (Fig. 4e). Next, we analyzed the
306 clustering ratios within the integrated UMAP plot for each of the five natural
307 human skin subpopulations of cells, including secretory papillary, secretory
308 reticular, proinflammatory, mesenchymal fibroblasts and pericytes (Fig. 4f).
309 The results revealed that secretory papillary fibroblasts and proinflammatory
310 fibroblasts corresponded to cluster #0', secretory reticular fibroblasts
311 corresponded to cluster #1', mesenchymal fibroblasts corresponded to cluster
312 #8', and pericytes corresponded to cluster #6'. We also investigated the Gene

313 Ontology (GO) terms enriched in cluster #0', which represents the papillary
314 fibroblast phenotype, and cluster #1', which represents the reticular
315 fibroblast phenotype. In cluster #1', GO terms related to collagen and elastic
316 fiber formation were particularly enriched, suggesting that the cells in cluster
317 #1' exhibited a phenotype closely resembling that of reticular fibroblasts (Fig.
318 4g).

319 In this study, we visualized the impact of vascularization. The results
320 indicated that 3D culture of keratinocytes and fibroblasts promotes the
321 restoration of the fibroblast subpopulations lost in 2D culture and that the
322 reconstitution of cell-to-cell communication with vascular endothelial cells
323 and skin cells is functional for the induction and maintenance of pericyte
324 subpopulations.

325

326 **Nutrient-poor culture conditions in the HSEs induce a senescent phenotype, which**
327 **is suppressed by ascorbic acid.**

328 Since blood vessels are central to maintaining organ homeostasis, vascular aging
329 is hypothesized to be a fundamental upstream factor of organismal aging[49,50]. During skin
330 aging, a reduction in blood vessels within the papillary layer and a decline in their

331 function are thought to contribute to the thinning of the epidermis and papillary dermis
332 due to impaired nutrient and paracrine factor supplies from vascular endothelial cells;
333 however, experimental evidence for this phenomenon remains limited[24–26]. To address
334 this limitation, we attempted to induce *in vitro a*ging in the ED and EDV models by
335 culturing them for 10 d in nutrient-poor medium (NP medium) with a low fetal bovine
336 serum concentration and depleted of bFGF and ascorbic acid. Moreover, ascorbic acid, a
337 well-evaluated antiaging material known for its antioxidant properties, ability to induce
338 epithelialization, and role as a coenzyme in collagen synthesis[51–53], was added to the NP
339 medium to evaluate its impact on HSE organization and skin functionality. HE staining
340 and immunohistological analysis revealed that skin tissue, including the epidermis,
341 dermis, and endothelial tubes with pericytes, was reconstructed even under NP culture
342 conditions (Fig. 5a). However, the number of Ki67-positive cells in the epidermal basal
343 cell layer was significantly lower in the EDV model than in the ED model (Fig. 5b). When
344 500 μM ascorbic acid was added, thickening of the CK5- and/or CK10- positive
345 epidermal layer and promotion of type 1 collagen deposition were observed in both the
346 ED and EDV models (Fig. 5a). In both the ED and EDV models, ascorbic acid increased
347 the number of Ki67-positive cells. Interestingly, when the ascorbic acid-treated ED and
348 EDV models were compared, the EDV model resulted in a significantly greater increase

349 in the number of Ki67-positive cells (Fig. 5b). In both the ED and EDV models, ascorbic
350 acid reduced TEWL and enhanced skin barrier function (Fig. 5c). 2D-FFT analysis
351 revealed that, compared with NP culture conditions alone, NP culture conditions with
352 ascorbic acid addition resulted in the CD31-positive vascular endothelial cells and the
353 surrounding type 1 collagen being oriented horizontally relative to the epidermal layer
354 (Fig. 5d). Furthermore, in the ascorbic acid-depleted EDV model, collagen fragments of
355 types 3 and 4 were deposited around CD31-positive endothelial tubes, suggesting
356 collagen degradation (Fig. 5a). NG2- and αSMA-positive pericytes were observed
357 surrounding the endothelial tubes regardless of the presence or absence of ascorbic acid
358 (Fig. 5a). Although no changes were detected in the ED model, skin elasticity was
359 significantly increased by ascorbic acid in the EDV model (Fig. 5e). In summary, NP
360 culture conditions enabled the *in vitro* replication of epidermal thinning, barrier disruption,
361 dermal elasticity reduction with imbalanced collagen synthesis and degradation, and
362 disordered vascular orientation, which are characteristics of *in vivo* human skin aging. It
363 was also demonstrated that ascorbic acid is effective in mitigating these aging-related
364 changes. These findings not only demonstrate that our HSE serves as a valuable tool for
365 evaluating the efficacy of functional molecules but also suggest that vascular endothelial
366 cells and pericytes play critical roles in the underlying mechanisms of action of these

molecules.

370 **Discussion**

371 Serial passaging often results in the loss of natural heterogeneous cell
372 characteristics and functions due to selective pressures caused by the medium and the
373 extracellular environment, representing a major obstacle to *in vitro r*esearch[29,54]. In this
374 study, we demonstrated that the heterogeneity of dermal mesenchymal cells, such as
375 papillary and reticular layer fibroblasts and pericytes, in natural human skin can be
376 reproduced via the reconstruction of an HSE using NHEKs, NHDFs, and HUVECs that
377 have undergone serial passaging. In particular, the EDV model containing a pericyte-like
378 subpopulation significantly improved skin and vascular tissue structure, barrier function,
379 and elasticity, enabling functional evaluation according to human clinical protocols.
380 Furthermore, we demonstrated that nutrient depletion can partially model skin aging,
381 making it a viable tool for evaluating the effectiveness of materials and elucidating new
382 mechanisms of action. Our HSE, which reproduces fibroblast heterogeneity by using
383 stably available primary culture cells, provides an alternative model to animal
384 experiments that can be used to analyze the mechanisms controlling skin physiological
385 functions based on cell-to-cell communication.

386 Fibroblast subpopulations differentiated from pluripotent fibroblasts during
387 embryonic development have their own distinct distributions and physiological functions,

388 such as the potential to differentiate into dermal papilla cells, APM cells, and adipocytes[55].
389 Papillary fibroblasts play important roles in wound healing functions such as re-
390 epithelialization and collagen synthesis. Furthermore, it has been reported that papillary
391 fibroblasts derived from elderly donors have reduced proliferation ability and KGF
392 secretion levels, suggesting that this effect may involve loss of the papillary dermis, loss
393 of elasticity, and deformation of skin texture due to aging[27,28]. In fact, recent scRNA-seq
394 analyses of human skin revealed changes in fibroblast subpopulations in the skin due to
395 aging and disease, suggesting the possibility of developing new therapeutic strategies by
396 controlling fibroblast heterogeneity[11,13,56]. Animal experiments using gene modification
397 techniques have demonstrated that epidermal Wnt signals are involved in the induction
398 of differentiation of the papillary fibroblast lineage and have shown that intervention in
399 dermal fibroblast subpopulations controls skin morphogenesis and functionality[55].
400 However, due to the lack of appropriate *in vitro* research models and to ethical restrictions
401 to clinical *in vivo* studies, the prospects for applying *in vitro* findings for human fibroblast
402 heterogeneity to *in vivo* health care are unclear. In our HSE, fibroblasts induced by three-
403 dimensional culture were not only in the G1 phase but also differentiated into papillary,
404 reticular, and mesenchymal fibroblast-like populations, exhibiting properties similar to
405 those of native skin fibroblasts. Interestingly, cells positive for FAP, a marker for papillary

406 fibroblasts, were present near the epidermal-dermal junction in both the ED and EDV
407 models, but CD39-positive cells were observed only in the EDV model. This observation
408 suggests that keratinocyte-fibroblast communication is required for the induction and
409 maintenance of papillary fibroblast differentiation and that some subpopulations, such as
410 CD39-positive cells, may require interaction with vascular endothelial cells. In the future,
411 by elucidating the mechanisms controlling human fibroblast heterogeneity via cell
412 tracking and spatiotemporal gene expression control techniques, our HSE will contribute
413 to the development of cell therapies for wound healing and aging.

414 In addition to papillary and reticular fibroblasts, perivascular mesenchymal cells
415 such as dermal stem cells and pericytes play important roles in skin morphogenesis and
416 function. Pericytes play an important role as the major source of ECM production during
417 tissue regeneration in many organs[57,58]. Additionally, in a previous study, HSEs
418 reconstructed using human pericytes and fibroblasts separated by flow cytometry
419 promoted the proliferation of epidermal basal cells through LAMA5 expression by
420 pericytes[29]. In our EDV model, we also confirmed that epithelialization and dermal ECM
421 synthesis were promoted with the emergence of a pericyte-like population. However, our
422 HSE is unique in that it does not require fresh human skin and allows the construction of
423 a model containing NG2- and αSMA-positive pericytes in a relatively simple process

424 from commercially available subcultured cells. *In vivo*, pericytes are a heterogeneous cell
425 population, and even pericytes from the same tissue may originate from multiple
426 sources[59,60]. Integrative analysis of scRNA-seq data from natural human skin and our
427 HSEs revealed that although the pericyte-like population in HSEs clustered with human
428 pericytes within the same subpopulation, their distributions on the UMAP plot only
429 partially overlapped. At the very least, the induced pericyte-like cluster 14 replicates well-
430 known *in vivo* angiogenic processes through interactions with endothelial cells, such as
431 VEGFB and PGF signaling via VEGFR1, and basement membrane-mediated interactions
432 between laminins and integrins[61–63]. These results suggest that the pericytes in our HSE
433 partially replicate certain populations and functions of human pericytes, although the
434 origin of this cell lineage and the mechanisms driving its induction remain unclear. Cell
435 tracking experiments using fluorescent dyes or genetic modifications targeting HSE
436 constituent cells could contribute to elucidating the origins and differentiation
437 mechanisms of human pericytes.

438 In addition to replicating the heterogeneity of dermal mesenchymal cells, the
439 EDV model significantly improved dermal elasticity as well as skin barrier function.
440 This improvement in dermal elasticity is attributed to the active ECM synthesis
441 functionality of pericytes compared with other subpopulations, as well as the autonomous

442 recapitulation of oriented collagen fiber formation along endothelial tubes. Furthermore,
443 we found that culture under nutrient-poor conditions enabled the HSE model to replicate
444 the phenotype of aged skin, including epidermal barrier dysfunction due to reduced
445 proliferation of basal keratinocytes, diminished dermal elasticity due to decreased
446 collagen synthesis, increased collagen degradation by MMPs, and loss of vascular
447 orientation. In natural human skin, oxidative stress and dermal ECM degradation are
448 thought to cause vascular atrophy and reduced vascular density, leading to depletion of
449 nutrient and oxygen supplies to the papillary dermis and epidermis, which contributes to
450 aging. Our findings support this hypothesis. In our nutrient-poor HSEs, a reduction in
451 vascular density was not observed, which is likely attributed to VEGF in the medium
452 continuously inducing angiogenesis. Ascorbic acid, which functions as both an
453 antioxidant and a coenzyme for 2-oxoglutarate-dependent dioxygenases, has been
454 supported by substantial evidence as an effective skin antiaging agent. However, the
455 effects of ascorbic acid on the vascular endothelium and perivascular mesenchymal cells,
456 as well as its impact on skin mechanical properties, remain unclear. Our findings revealed
457 that ascorbic acid increased collagen synthesis in both the ED and EDV models but
458 significantly improved skin viscoelasticity only in the EDV model, indicating that
459 vascular endothelial cells and pericytes play crucial roles in regulating skin elasticity and

460 serve as target cells for ascorbic acid. Decreased skin elasticity not only reduces quality
461 of life due to skin deformation such as wrinkling and sagging[64,65] but also causes skin
462 tearing and is therefore a serious clinical issue in an aging society[66,67]. In summary, our
463 model is valuable for studying cell-to-cell communication between the vasculature and
464 skin, and it has the potential to contribute to societal improvements in quality of life
465 through the development of vascular-targeted therapies for aging and disease.

466 In conclusion, we reconstructed HSEs that reproduce skin fibroblast
467 heterogeneity, tissue structure, and physiological function in natural human skin. Further
468 research, such as elucidating the mechanisms controlling fibroblast heterogeneity,
469 evaluating the impact of each cell population on skin morphogenesis, and identifying
470 drugs that can control the decrease or increase in specific fibroblast populations, will
471 provide new insights into the fields of basic science, personalized medicine, and health
472 care. Our model will contribute to the reduction of animal experiments and the sustainable
473 growth of the health care industry as a versatile research model that can evaluate skin
474 functionality as an alternative to clinical research. In the future, it is expected that HSEs
475 that highly replicate skin cell heterogeneity and function will be developed by improving
476 their vascular structure through perfusion culture and providing cell-to-cell
477 communication via organoids such as the integumentary organ system and the nervous

system.

480 **Methods**

481

482 **Cell culture**

483 Normal human epidermal keratinocytes (NHEKs) were purchased from
484 KURABO Industries Ltd. (Osaka, Japan) and were maintained in HuMedia-KG2
485 (KURABO). Normal human dermal fibroblasts (NHDFs) were purchased from
486 KURABO and maintained in Dulbecco's modified Eagle's medium (Thermo Fisher
487 Scientific, MA, USA) supplemented with 10% fetal bovine serum (Corning, NY, USA),
488 100 units ml^{-1} penicillin, and 100 μg ml^{-1} streptomycin (Thermo Fisher Scientific).
489 Human umbilical vein endothelial cells (HUVECs) were purchased from KURABO and
490 maintained in HuMedia-EG2 (KURABO). All cells were seeded into 150-mm dishes and
491 grown in a humidified atmosphere of 5% CO_2 at 37 °C.

492

493 **Reconstruction of the tension homeostatic skin (THS) model**

494 The THS model was generated via the following procedure. A total of 24×10^5
495 NHDFs and 30×10^5 HUVECs were resuspended in 2.4 ml of 1.25 mg ml^{-1} bovine
496 dermis-derived native collagen solution (KOKEN CO. Ltd., Tokyo, Japan) that was
497 mixed with 1× DMEM (Thermo Fisher Scientific), 15 mM HEPES (Dojindo, Kumamoto,

498 Japan), 10 mM $NaHCO_3$ (FUJIFILM Wako Pure Chemical Corporation), and 5 mg ml^{-1}

499 fibrinogen from bovine plasma type I-S (Merck KGaA, Darmstadt, Germany); then, the

500 cells were plated in a high-density translucent-membrane cell culture insert (0.4-μm pore

501 size) (Corning, NY, USA) in 6-well plates. After solidification, the dermal equivalents

502 were held in place by a Snapwell culture insert (Corning). NHEKs were seeded at a

503 density of 1.1×10^6 cells/well on fixed dermal equivalents, and they were cultured in

504 growth medium under submersion conditions for 4 d in a humidified atmosphere at 37 °C

505 with 5% CO_2 and 12.5% O_2. After maintenance in a submersion culture, the HSEs were

506 exposed to the air-liquid interface in a humidified atmosphere at 37 °C with 5% CO_2. The

507 growth medium for culturing HSEs consisted of DMEM supplemented with 10% FBS,

508 1% penicillin/streptomycin, 5 μg ml^{-1} insulin (FUJIFILM Wako Pure Chemical

509 Corporation), 500 μM ascorbic acid (FUJIFILM Wako Pure Chemical Corporation), 10

510 ng ml^{-1} bFGF (PeproTech, NJ, USA), 1 μM hydrocortisone (FUJIFILM Wako Pure

511 Chemical Corporation), and 5 nM VEGF 165 Human Recombinant (PeproTech) and was

512 replaced with fresh medium every 48 to -72 h.

513

514 **H&E staining and immunohistochemistry**

515 For histological analysis, skin equivalents from three independent experiments

516 were fixed with 4% formaldehyde and embedded in paraffin or Tissue-Tek O.C.T.
517 compound (Sakura Finetek Japan Co., Ltd., Tokyo, Japan). Hematoxylin-eosin staining
518 was performed on paraffin sections (10 μm thick). The stained sections were observed
519 via AxioScan.Z1 (Carl Zeiss, Oberkochen, Germany). For fluorescence
520 immunohistochemistry, frozen sections (10 and 50 μm) and paraffin sections (10 μm)
521 were prepared and stained as previously described[38]. Details of the primary and secondary
522 antibodies and associated epitope recovery methods are included in Table 1. All
523 fluorescence microscopy images were captured with an AxioScan.Z1 or LSM 900
524 confocal microscope (Carl Zeiss).
525
526 **Quantitative analysis of epidermal cell proliferation.**
527 The proliferation rate of epidermal cells was quantified by counting
528 keratinocytes with Ki67-positive nuclei located at the basal or immediately suprabasal
529 epidermis. The measurement area was a total of 3 images obtained by randomly acquiring
530 three z-stack images of 1000 × 340 × 10 μm from HSE tissues that were derived from
531 three different wells.
532
533 **Quantification of blood vessel alignment**

534 Anisotropic alignment of endothelial tubes and collagen fibers was assessed via two-
535 dimensional fast Fourier transform (2D-FFT) analysis, as previously described[68]. Briefly,
536 uncompressed images of endothelial tubes labeled with anti-CD31 antibody and basement
537 membranes labeled with anti-COL1 antibody were analyzed with the FFT function of
538 ImageJ, and the radial summation of the FFT frequency plot was calculated via the Oval
539 profile plug-in. The degree of fiber alignment was reflected by the shape and height of
540 the major peak in the FFT alignment plot. Images with oriented blood vessels resulted in
541 a prominent peak centered at the principal axis of fiber alignment, whereas images with
542 unaligned actin fibers resulted in an alignment plot with a broad peak or no peak.
543
544 **Single-cell RNA-seq library preparation**
545 NHEKs, NHDFs, and HUVECs cultured to a subconfluent state were harvested
546 through trypsinization according to the product protocol. Briefly, the cells were washed
547 with HEPES-buffered solution (Kurabo) to remove the medium and treated with 0.025%
548 trypsin/EDTA solution (Kurabo) for 3–7 min, followed by the addition of a trypsin-
549 neutralizing solution (Kurabo) and centrifugation to obtain a cell pellet. Constituent HSE
550 cells were harvested through enzymatic digestion. On day 14 of air-liquid interface
551 culture, the epidermis and dermis of the HSE were mechanically separated using forceps.

552 The epidermal layer was enzymatically dissociated with 0.025% trypsin/EDTA solution,
553 while the dermal layer was incubated in 10% FBS-supplemented DMEM containing 5000
554 U/ml collagenase type 1 (Worthington Biochemical Corp., NJ, USA) in a 37 °C water
555 bath. The resulting cell suspension was filtered through a 70-µm cell strainer to remove
556 debris and centrifuged to obtain a cell pellet. Single-cell RNA sequencing was conducted
557 using the Chromium Next GEM Single Cell 3′ Kit v3.1, Chromium Next GEM Chip G
558 Single Cell Kit, and Dual Index Kit TT Set A (10x Genomics) according to the
559 manufacturer's protocol (CG000315 Rev E). Cell viability and count were assessed using
560 a Countess 3 Automated Cell Counter following trypan blue staining and visual inspection.
561 The cell suspension was processed on a chromium controller for gel bead-in-emulsion
562 (GEM) generation, where polyadenylated mRNA was reverse transcribed to cDNA and
563 uniquely barcoded. The cDNA was subjected to amplification, quality assessment via
564 electrophoresis, and library preparation involving fragmentation, end-repair, A-tailing,
565 adaptor ligation, and PCR amplification. Library quality was evaluated using Agilent's
566 High Sensitivity D5000 ScreenTape system, and the DNA concentration was measured
567 with a Qubit 1X dsDNA HS Assay Kit on a Qubit 4 Fluorometer. Libraries were
568 sequenced on an Illumina NovaSeq 6000 with PE150, generating approximately 120 Gb
569 of data per sample from ~800 million reads.

570

571 **Single-cell RNA-seq data processing: *In vitro* skin data**

572 FASTQ reads of 10× scRNA sequencing data were processed with the hg38
573 reference genome via Cell Ranger (v7.1.0)[69]. A total of 27,082 cells passed the quality
574 control steps. The processed matrices of different batches were merged, and the following
575 analyses were performed via SEURAT-1 (v5.0.3). Cells with 1,000 to 8,000 RNA features
576 and mitochondrial RNA contents of less than 7% were selected. The selected expression
577 matrix was normalized by the total number of UMIs per cell and was log-transformed.

578 The filtered dataset was split into original sample identities via the Split Object
579 function, followed by data log normalization of UMI counts and identification and the
580 identification of 2000 more variable genes per sample.

581 The integrated data were then used for standard cell clustering and visualization with
582 Seurat, which uses the 2000 most variable genes of the integrated dataset as input. Next,
583 we used the function FindIntegrationAnchors with default parameters and 30 canonical
584 correlation analysis (CCA) dimensions to identify the integration anchors between our
585 five datasets. These anchors were subsequently used for integration via the IntegrateData
586 function, again with the first 30 CCA dimensions and default parameters.

587 The integrated data were then used for standard cell clustering and visualization

588 with Seurat, which uses the 2000 most variable genes of the integrated dataset as input.
589 First, the data were scaled via the ScaleData function, and principal component analysis
590 (PCA) dimensions were calculated via the RunPCA function. Next, unsupervised
591 clustering of the data was performed with the FindNeighbors and FindClusters functions.
592 For the FindNeighbors function, we used the first 30 PCA dimensions to construct a
593 shared nearest neighbor (SNN) graph for our dataset. Then, we clustered the cells with
594 the function FindClusters via a shared nearest neighbor (SNN) modularity optimization-
595 based clustering algorithm with a resolution of 0.7. Finally, for visualization, we used the
596 RunUMAP function with default parameters and 30 PCA dimensions.
597

598 **Single-cell RNA-seq data processing: *In vivo* skin data and data integration with *in***
599 ***vitro* skin data**

600 *In vivo* skin single-cell analysis was carried out via methods described in
601 previous studies[13]. After mapping cell types based on the expression of marker genes for
602 each cell type, we further explored the correspondence between the clusters and the four
603 fibroblast subpopulations mentioned in the original paper. This was accomplished by
604 examining the expression of marker genes for papillary fibroblasts and reticular
605 fibroblasts, as well as the top enriched Gene Ontology (GO) terms for the four fibroblast

clusters. Consistent with previous studies, Cluster 1 was classified as secretory-reticular, Cluster 2 as proinflammatory, Cluster 3 as secretory-papillary, and Cluster 9 as mesenchymal.

To integrate *in vitro* and *in vivo* data, cells annotated as vascular ECs, pericytes, keratinocytes, and fibroblasts were initially extracted from the *in vivo* dataset. The cells from each sample were filtered under specific conditions: for *in vitro* samples, cells with 1000 to -8000 RNA features and mitochondrial RNA contents of less than 7% were selected; for *in vivo* samples, the criteria were fewer than 7500 RNA features and mitochondrial RNA contents of less than 5%. Following this, normalization was performed via the SCTransform method. Using Seurat's default approach, the top 2000 genes with the most variability from each dataset were extracted. All the data were then combined to compute principal component analysis (PCA) dimensions, and batch effects between datasets were mitigated using the Harmony algorithm's RunHarmony unction (parameters set to theta=1, max.iter.harmony=10). Unsupervised clustering of the data was subsequently performed via the FindNeighbors and FindClusters functions. Finally, for visualization purposes, the RunUMAP function was employed with default parameters and 30 PCA dimensions.

624 **Cell–to-cell communication analysis**

625 To analyze the estimated intercellular interactions established by different cell
626 types present in artificial skin, we utilized R CellChat3 (v1.6.1)[70]. This tool can
627 quantitatively infer and analyze intercellular communication networks from scRNA-seq
628 data and contains ligand-receptor interaction databases (http://www.cellchat.org/). In our
629 approach, pairwise comparisons across all cell clusters present in the artificial skin dataset
630 were conducted, and the analysis was performed using the default parameters set by the
631 tool.

632

633 **Evaluation of the epidermal barrier function of HSEs via TEWL measurement**

634 Trans-epidermal water loss (TEWL) was measured in the HSEs (n = 4) using a
635 Tewameter TM HEX (Courage & Khazaka electronic, Cologne, Germany) according to
636 the instruction manual. Prior to collection, the skin equivalent was incubated inside the
637 biosafety cabinet for 15 min to allow equilibration to the ambient temperature and
638 humidity of the room. The measurement was repeated three times, and the average and
639 standard deviation of each well were calculated.

640

641 **Measurements of skin elasticity**

642 Skin elasticity was determined via a noninvasive, *in vivo* suction skin elasticity
643 meter, the Cutometer MPA 580 (Courage & Khazaka electronic). The measurement
644 conditions were the same as those used in previously reported human clinical studies[46].
645 Briefly, with a 2-mm probe, a negative pressure of 400 mbar was applied to the HSEs for
646 a period of 2 s, followed by 2 s of relaxation time, and the ratio of immediate retraction
647 (Ur) and the ability of redeformation of the skin (Ua) to final distension (Uf) was analyzed
648 (R2 = Ua/Uf, R7 = Ur/Uf).
649
650 **Nutrient-poor culture of HSEs and evaluation of their responsiveness to ascorbic**
651 **acid**
652 All HSEs were treated with nutrient-poor medium (DMEM supplemented with
653 1% FBS, 1% penicillin/streptomycin, 5 μg ml^{-1} insulin, and 1 μM hydrocortisone) at the
654 air-liquid interface on day 3 and maintained for 12 d. Then, 500 μM ascorbic acid was
655 added to the HSEs cultured at the air-liquid interface on day 5 and maintained for 10 d.
656
657 **Statistics and reproducibility**
658 Microsoft Excel (Microsoft, Redmond, WA, USA) and BellCurve for Excel
659 were used for statistical analysis. All values are expressed as the means ± standard

660 deviations (SDs). Analysis of the samples was performed at least in triplicate, and the

661 results were averaged. Differences between groups were considered significant at

662 $P<0.05$. All the experiments were repeated at least three times.

663

664 **Data availability**

665 scRNA-seq data from this study have been deposited into the Sequence Read

666 Archive (SRA) database under the BioProject ID. PRJNA1191968. All data are

667 available from the corresponding authors upon reasonable request.

668

References

1. Jiang, T.-X. *et al.* Integument pattern formation involves genetic and epigenetic controls: feather arrays simulated by digital hormone models HHS Public Access. *Int J Dev Biol* **48**, 117–135 (2004).
2. Driskell, R. R., Jahoda, C. A. B., Chuong, C., Watt, F. M. & Horsley, V. Defining dermal adipose tissue. *Exp Dermatol* **23**, 629–631 (2014).
3. Meigel, W. N., Gay, S. & Weber, L. Dermal architecture and collagen type distribution. *Archives for Dermatological Research* **259**, 1–10 (1977).
4. Braverman, I. M. The cutaneous microcirculation. *Journal of Investigative Dermatology Symposium Proceedings* **5**, 3–9 (2000).
5. K. Langer. On the anatomy and physiology of the skin. I. The cleavability of the cutis. (Translated from Langer, K. (1861). Zur Anatomie und Physiologie der Haut. I. Uber die Spaltbarkeit der Cutis. Sitzungsbericht der Mathematisch-naturwissenschaftlichen Classe der Kaiserlichen Academie der Wissenschaften, 44, 19.). *Br J Plast Surg* **31**, 3–8 (1978).
6. Di Carlo, S. E. & Peduto, L. The perivascular origin of pathological

687 fibroblasts. *Journal of Clinical Investigation* vol. 128 54–63 Preprint at
688 https://doi.org/10.1172/JCI93558 (2018).
689 7. Ganier, C., Rognoni, E., Goss, G., Lynch, M. & Watt, F. M. Fibroblast
690 Heterogeneity in Healthy and Wounded Skin. *Cold Spring Harb*
691 *Perspect Biol* a041238 (2022) doi:10.1101/cshperspect.a041238.
692 8. Amiri, N., Golin, A. P., Jalili, R. B. & Ghahary, A. Roles of cutaneous
693 cell-cell communication in wound healing outcome: An emphasis on
694 keratinocyte-fibroblast crosstalk. *Experimental Dermatology* vol. 31
695 475–484 Preprint at https://doi.org/10.1111/exd.14516 (2022).
696 9. Hsu, Y. C., Li, L. & Fuchs, E. Emerging interactions between skin stem
697 cells and their niches. *Nature Medicine* vol. 20 847–856 Preprint at
698 https://doi.org/10.1038/nm.3643 (2014).
699 10. Russo, B., Brembilla, N. C. & Chizzolini, C. Interplay between
700 keratinocytes and fibroblasts: A systematic review providing a new
701 angle for understanding skin fibrotic disorders. *Frontiers in*
702 *Immunology* vol. 11 Preprint at
703 https://doi.org/10.3389/fimmu.2020.00648 (2020).
704 11. Tabib, T., Morse, C., Wang, T., Chen, W. & Lafyatis, R. SFRP2/DPP4 and

705 FMO1/LSP1 Define Major Fibroblast Populations in Human Skin.
706 *Journal of Investigative Dermatology* **138**, 802–810 (2018).
707 12. Philippeos, C. *et al.* Spatial and Single-Cell Transcriptional Profiling
708 Identifies Functionally Distinct Human Dermal Fibroblast
709 Subpopulations. *Journal of Investigative Dermatology* **138**, 811–825
710 (2018).
711 13. Solé-Boldo, L. *et al.* Single-cell transcriptomes of the human skin reveal
712 age-related loss of fibroblast priming. *Commun Biol* **3**, 1–12 (2020).
713 14. Deng, C. C. *et al.* Single-cell RNA-seq reveals fibroblast heterogeneity
714 and increased mesenchymal fibroblasts in human fibrotic skin diseases.
715 *Nat Commun* **12**, 1–16 (2021).
716 15. He, H. *et al.* Single-cell transcriptome analysis of human skin identifies
717 novel fibroblast subpopulation and enrichment of immune subsets in
718 atopic dermatitis. *Journal of Allergy and Clinical Immunology* **145**,
719 1615–1628 (2020).
720 16. Reynolds, G. *et al.* Developmental cell programs are co-opted in
721 inflammatory skin disease. *Science (1979)* **371**, (2021).
722 17. Cha, J. & Lee, I. Single-cell network biology for resolving cellular

723 heterogeneity in human diseases. *Exp Mol Med* **52**, 1798–1808 (2020).

724 18. Rittie, L. & Fisher, G. J. Natural and Sun-Induced Aging of Human

725 Skin. *Cold Spring Harb Perspect Med* **5**, a015370–a015370 (2015).

726 19. Montagna, W. & Carlisle, K. Structural Changes in Aging Human Skin.

727 *Journal of Investigative Dermatology* **73**, 47–53 (1979).

728 20. Luebberding, S., Krueger, N. & Kerscher, M. Age - related changes in

729 skin barrier function – Quantitative evaluation of 150 female subjects.

730 *Int J Cosmet Sci* **35**, 183–190 (2013).

731 21. Manuskiatti, W., Schwindt, D. A. & Maibach, H. I. Influence of Age,

732 Anatomic Site and Race on Skin Roughness and Scaliness. *Dermatology*

733 **196**, 401–407 (1998).

734 22. Lavker, R. M., Zheng, P. & Dong, G. Morphology of Aged Skin. *Clin*

735 *Geriatr Med* **5**, 53–67 (1989).

736 23. Naylor, E. C., Watson, R. E. B. & Sherratt, M. J. Molecular aspects of

737 skin ageing. *Maturitas* vol. 69 249–256 Preprint at

738 https://doi.org/10.1016/j.maturitas.2011.04.011 (2011).

739 24. Bonta, M., Daina, L. & Mușiu, G. The process of ageing reflected by

740 histological changes in the skin. *Rom J Morphol Embryol* **54**, 797–804

741 (2013).

742 25. Braverman, I. M. & Keh-Yen, A. Ultrastructure of the Human Dermal
743 Microcirculation. III. The Vessels in the Mid- and Lower Dermis and
744 Subcutaneous Fat. *Journal of Investigative Dermatology* **77**, 297–304
745 (1981).

746 26. Gunin, A. G., Petrov, V. V., Vasilieva, O. V. & Golubtsova, N. N. Age-
747 related changes of blood vessels in the human dermis. *Advances in*
748 *Gerontology* **5**, 65–71 (2015).

749 27. Mine, S., Fortunel, N. O., Pageon, H. & Asselineau, D. Aging alters
750 functionally human dermal papillary fibroblasts but not reticular
751 fibroblasts: A new view of skin morphogenesis and aging. *PLoS One* **3**,
752 (2008).

753 28. Sriram, G., Bigliardi, P. L. & Bigliardi-Qi, M. Fibroblast heterogeneity
754 and its implications for engineering organotypic skin models in vitro.
755 *Eur J Cell Biol* **94**, 483–512 (2015).

756 29. Paquet-Fifield, S. *et al.* A role for pericytes as microenvironmental
757 regulators of human skin tissue regeneration. *Journal of Clinical*
758 *Investigation* **119**, 2795–2806 (2009).

30. Salzer, M. C. *et al.* Identity Noise and Adipogenic Traits Characterize Dermal Fibroblast Aging. *Cell* **175**, 1575-1590.e22 (2018).

31. Dubois, A., Gopee, N., Olabi, B. & Haniffa, M. Defining the Skin Cellular Community Using Single-Cell Genomics to Advance Precision Medicine. *Journal of Investigative Dermatology* **141**, 255–264 (2021).

32. Bassi, G., Grimaudo, M. A., Panseri, S. & Montesi, M. Advanced multi-dimensional cellular models as emerging reality to reproduce In Vitro the human body complexity. *International Journal of Molecular Sciences* vol. 22 1–28 Preprint at https://doi.org/10.3390/ijms22031195 (2021).

33. Ferreira, M., Matos, A., Couras, A., Marto, J. & Ribeiro, H. Overview of Cosmetic Regulatory Frameworks around the World. *Cosmetics* vol. 9 Preprint at https://doi.org/10.3390/cosmetics9040072 (2022).

34. Voelkl, B. *et al.* Reproducibility of animal research in light of biological variation. *Nature Reviews Neuroscience* vol. 21 384–393 Preprint at https://doi.org/10.1038/s41583-020-0313-3 (2020).

35. Lynch, M. D. & Watt, F. M. Fibroblast heterogeneity: implications for human disease. *Journal of Clinical Investigation* **128**, 26–35 (2018).

36. Marx, V. Closing in on cancer heterogeneity with organoids. *Nat Methods* **21**, 551–554 (2024).

37. Hong, Z. X. *et al.* Bioengineered skin organoids: from development to applications. *Mil Med Res* **10**, 1–17 (2023).

38. Toyoshima, K. E. *et al.* Fully functional hair follicle regeneration through the rearrangement of stem cells and their niches. *Nat Commun* **3**, (2012).

39. Nebuloni, F., Morgan, J., Walsh, E. J. & Cook, P. R. A platform for modular assembly and feeding of micro-organoids on standard Petri dishes. *Biol Open* **12**, (2023).

40. Ibrahim, M. & Richardson, M. K. Beyond organoids: In vitro vasculogenesis and angiogenesis using cells from mammals and zebrafish. *Reproductive Toxicology* **73**, 292–311 (2017).

41. Bell, E., Ivarsson, B. & Merrill, C. Production of a tissue-like structure by contraction of collagen lattices by human fibroblasts of different proliferative potential in vitro. *Proceedings of the National Academy of Sciences* **76**, 1274–1278 (1979).

42. Nusgens, B., Merrill, C., Lapiere, C. & Bell, E. Collagen biosynthesis by

795 cells in a tissue equivalent matrix in vitro. *Coll Relat Res* **4**, 351–63
796 (1984).
797 43. Kimura, S. *et al.* Tissue-scale tensional homeostasis in skin regulates
798 structure and physiological function. *Commun Biol* **3**, (2020).
799 44. Ichijo, R. *et al.* Vasculature atrophy causes a stiffened
800 microenvironment that augments epidermal stem cell differentiation in
801 aged skin. *Nat Aging* **2**, 592–600 (2022).
802 45. Dulauroy, S., Di Carlo, S. E., Langa, F., Eberl, G. & Peduto, L. Lineage
803 tracing and genetic ablation of ADAM12 + perivascular cells identify a
804 major source of profibrotic cells during acute tissue injury. *Nat Med* **18**,
805 1262–1270 (2012).
806 46. Ezure, T., Hosoi, J., Amano, S. & Tsuchiya, T. Sagging of the cheek is
807 related to skin elasticity, fat mass and mimetic muscle function. *Skin*
808 *Research and Technology* **15**, 299–305 (2009).
809 47. Jin, S., Plikus, M. V. & Nie, Q. CellChat for systematic analysis of cell–
810 cell communication from single-cell transcriptomics. *Nat Protoc* (2024)
811 doi:10.1038/s41596-024-01045-4.
812 48. Butler, A., Hoffman, P., Smibert, P., Papalexi, E. & Satija, R. Integrating

813 single-cell transcriptomic data across different conditions, technologies,
814 and species. *Nat Biotechnol* **36**, 411–420 (2018).
815 49. Rastogi, C. *et al.* Counteracting age-related VEGF signaling
816 insufficiency promotes healthy aging and extends life span. *Science*
817 *(1979)* **373**, E3692–E3701 (2021).
818 50. Le Couteur, D. G. & Lakatta, E. G. A Vascular Theory of Aging. *J*
819 *Gerontol A Biol Sci Med Sci* **65A**, 1025–1027 (2010).
820 51. Masaki, H. Role of antioxidants in the skin: Anti-aging effects. *J*
821 *Dermatol Sci* **58**, 85–90 (2010).
822 52. Boo, Y. C. Ascorbic Acid (Vitamin C) as a Cosmeceutical to Increase
823 Dermal Collagen for Skin Antiaging Purposes: Emerging Combination
824 Therapies. *Antioxidants* **11**, (2022).
825 53. Pullar, J. M., Carr, A. C. & Vissers, M. C. M. The roles of vitamin C in
826 skin health. *Nutrients* **9**, (2017).
827 54. Korosec, A. *et al.* Lineage Identity and Location within the Dermis
828 Determine the Function of Papillary and Reticular Fibroblasts in
829 Human Skin. *Journal of Investigative Dermatology* **139**, 342–351 (2019).
830 55. Driskell, R. R. *et al.* Distinct fibroblast lineages determine dermal

architecture in skin development and repair. *Nature* **504**, 277–281 (2013).

56. He, H. *et al.* Single-cell transcriptome analysis of human skin identifies novel fibroblast subpopulation and enrichment of immune subsets in atopic dermatitis. *Journal of Allergy and Clinical Immunology* **145**, 1615–1628 (2020).

57. Kramann, R. *et al.* Perivascular Gli1+ progenitors are key contributors to injury-induced organ fibrosis. *Cell Stem Cell* **16**, 51–66 (2015).

58. Greenhalgh, S. N., Iredale, J. P. & Henderson, N. C. Origins of fibrosis: Pericytes take centre stage. *F1000Prime Rep* **5**, (2013).

59. Dias Moura Prazeres, P. H. *et al.* Pericytes are heterogeneous in their origin within the same tissue. *Developmental Biology* vol. 427 6–11 Preprint at https://doi.org/10.1016/j.ydbio.2017.05.001 (2017).

60. Goss, G., Rognoni, E., Salameti, V. & Watt, F. M. Distinct Fibroblast Lineages Give Rise to NG2+ Pericyte Populations in Mouse Skin Development and Repair. *Front Cell Dev Biol* **9**, 1–18 (2021).

61. Greenberg, J. I. *et al.* A role for VEGF as a negative regulator of pericyte function and vessel maturation. *Nature* **456**, 809–814 (2008).

62. Huang, H. Pericyte-endothelial interactions in the retinal microvasculature. *International Journal of Molecular Sciences* vol. 21 1–18 Preprint at https://doi.org/10.3390/ijms21197413 (2020).

63. Bergers, G. & Song, S. The role of pericytes in blood-vessel formation and maintenance. *Neuro-Oncology* vol. 7 452–464 Preprint at https://doi.org/10.1215/S1152851705000232 (2005).

64. Haydont, V., Bernard, B. A. & Fortunel, N. O. Age-related evolutions of the dermis: Clinical signs, fibroblast and extracellular matrix dynamics. *Mechanisms of Ageing and Development* vol. 177 150–156 Preprint at https://doi.org/10.1016/j.mad.2018.03.006 (2019).

65. Taieb, C., Rahhali, N., Moingeon, V., Perez-Cullell, N. & Sibaud, V. CosmeceutiQoL: A tool for assessing dermo-cosmetic products' impact on quality of life. *Journal of Cosmetic and Laser Therapy* **14**, 18–23 (2012).

66. LeBlanc, K. A. & Christensen, D. Demystifying skin tears, part 1. *Nursing (Brux)* **40**, 62–63 (2010).

67. Roberts, M. J. Preventing and Managing Skin Tears. *Journal of Wound, Ostomy & Continence Nursing* **34**, 256–259 (2007).

68. Aw, W. Y., Heck, B. W., Joyce, B. & Devenport, D. Transient Tissue-Scale Deformation Coordinates Alignment of Planar Cell Polarity Junctions in the Mammalian Skin. *Current Biology* **26**, 2090–2100 (2016).

69. Hao, Y. *et al.* Dictionary learning for integrative, multimodal and scalable single-cell analysis. *Nat Biotechnol* **42**, 293–304 (2024).

70. Jin, S. *et al.* Inference and analysis of cell-cell communication using CellChat. *Nat Commun* **12**, 1–20 (2021).

878 **Acknowledgments:** We thank laboratory members at the Institute of Advanced
879 Biomedical Engineering and Science, TWIns, Tokyo Women's Medical University. We
880 also thank Mr. M. Hashimoto, Y. Hayashi, and all the members of Rohto Pharmaceutical
881 Co., Ltd., for their support and encouragement in this project. We would like to thank
882 Rohto Pharmaceutical Co., Ltd., for funding support.

883

884 **Author contributions:** S.K., S.S. and T.S. designed the research plans; S.K. and S.Y.
885 performed the experiments; S.K., S.S., T.K., S.Y., M.H., and T.S. discussed the results;
886 and S.K. and S.Y. wrote the manuscript.

887

888 **Competing interests:** S.K., S.Y., and M.H. are employees of Rohto Pharmaceutical Co.,
889 Ltd.. T.S., S.S, and T.K have collaborated with Rohto Pharmaceutical Co., Ltd. and
890 received research funding from the company. A part of the study was financially
891 supported by Rohto Pharmaceutical Co., Ltd. under a collaboration contract with Tokyo
892 Women's Medical University.

893

894 **Author information:** Correspondence and requests for materials should be addressed to
895 S.K. (skimura@rohto.co.jp).

896

897 **Figure 1 Tricellular communication regulates skin and vascular organization.**

898 (a) Schematic representation of the construction method of HSEs. (b) Macroscopic

899 images of the constructed HSEs. The abbreviations for the HSE and the constituent cell

900 types are listed at the top of each image. Scale bars, 1 mm. (c) H&E staining images of

901 human skin and the HSEs at low (upper columns; scale bars, 200 μm) and high (lower

902 columns; scale bars, 50 μm) magnification. The arrowheads indicate the endothelial

903 tube. (d) Sirius Red-stained images of human skin and the HSEs; scale bars, 50 μm.

904

905 **Figure 2 Tricellular communication enhances skin barrier function and elasticity**

906 **by inducing self-organization.**

907 (a) Immunohistochemical analyses of human skin and HSEs for evaluation of

908 epithelialization. These samples were stained with CK5, CK10, CLDN1, FLG and Ki67

909 antibodies. The dotted lines indicate the boundary between the epidermis and dermis.

910 Scale bars, 50 μm. (b) Analysis of the Ki67-positive basal keratinocyte ratio in HSEs.

911 *$P < 0.001$, as assessed by Dunnett's test following two-way analysis of variance

912 (ANOVA; $P < 0.001$). (c) TEWL analysis of the ED and EDV models. *$P < 0.05$ and, as

913 assessed by two-tailed Student's t tests; error bars represent the standard deviation. (d)

914 Immunohistochemical analyses of human skin and HSEs for evaluation of angiogenesis

915 and dermal collagen synthesis. These samples were stained with CD31, COL4, vWF,
916 COL1 and COL3/4 antibodies. (e) Macroscopic image of CD31 and COL1 distribution
917 (upper column) and FFT analysis (lower columns) of the alignment of CD31-positive
918 endothelial tubes and COL1-positive type 1 collagen fiber in the EDV model. Scale
919 bars, 500 μm. (f) Skin deformation curves obtained from the ED model (upper panel)
920 and EDV model. (g) R7 factor evaluation of the ED and EDV models. *$P < 0.05$ and, as
921 assessed by two-tailed Student's t tests; error bars represent the standard deviation.
922
923 **Figure 3. The three-dimensional culture environment and cell-to-cell**
924 **communication replicate dermal mesenchymal cell heterogeneity *in vitro.***
925 (a) Immunohistochemical analyses of ED, EDV and human skin samples to evaluate the
926 existence and distribution of dermal mesenchymal cell subpopulations. These samples
927 were stained with the papillary fibroblast markers CD39 and FAP, the reticular
928 fibroblast markers CD36 and CD90, and the pericyte markers NG2 and αSMA. The
929 dotted lines indicate the boundary between the epidermis and dermis. Scale bars, 100
930 μm. (b) Illustration of the workflow for scRNA-seq data sampling and analysis. (c)
931 UMAP plot of scRNA-seq data for *in vitro* HSEs; the average expression of four cell-
932 type markers is projected onto the UMAP plot to identify cell populations. (d)

933 Distribution of fibroblast and pericyte cells under each of the three conditions. (e)
934 Cellular communication from vascular endothelial cells (ECs; Clusters #4 and #5) to
935 pericytes in Cluster #14 and to fibroblasts in Cluster #9. (f) Heatmap showing the
936 average expression levels of ECM-related genes across all fibroblasts under different
937 conditions.
938
939 **Figure 4 Analysis of the biological significance of fibroblast heterogeneity in HSEs**
940 **through integrated analysis of human scRNA-seq data.**
941 (a) UMAP plot of scRNA-seq data for integrating *in vitro* artificial skin and *in vivo* skin
942 data. (b) Average expression of established cell type markers was projected on the
943 UMAP plot to identify cell populations. Red indicates maximum gene expression,
944 whereas blue indicates low or no expression of a particular set of genes in log-
945 normalized UMI counts. (c) UMAP plot integrating scRNA-seq data from *in vitro* HSEs
946 and *in vivo* skin, showing the distribution of fibroblasts and pericytes across each of the
947 three *in vitro* conditions and the *in vivo* condition. (d) Cell cycle status of fibroblasts
948 under each condition. (e) UMAP plot showing the correspondence of the four fibroblast
949 subpopulations and pericytes defined by L. Solé-Boldo *et al*. (f) Proportion of cells from
950 each subpopulation as defined by L. Solé-Boldo *et al*. and their clustering into specific

951 clusters, as shown in Fig. 4e. (g) Enriched Gene Ontology (GO) terms in clusters #0'

952 and #1'.

953

954 **Figure 5 Nutrient-poor culture conditions in the HSEs induce a senescent phenotype,**

955 **which is suppressed by ascorbic acid.**

956 Histological analysis of skin tissue organization induced by ascorbic acid

957 supplementation in nutrient-poor cultured HSEs.These samples were stained with H&E,

958 CK5, CK10, CLDN1, FLG and Ki67 antibodies. The dotted lines indicate the boundary

959 between the epidermis and dermis. Scale bars, 50 μm. (b) Analysis of the Ki67-positive

960 basal keratinocyte ratio in HSEs. *$P < 0.001$, as assessed by two-tailed Student's t tests;

961 error bars represent the standard deviation.(c) TEWL analysis of the ED and EDV models.

962 *$P < 0.001$, as assessed by two-tailed Student's t tests; error bars represent the standard

963 deviation. (d) 2D-FFT analysis (lower columns) of the alignment of CD31-positive

964 endothelial tubes and COL1-positive type 1 collagen fiber in the EDV model. (e) R7

965 factor evaluation of the ED and EDV models. *$P < 0.01$ and, as assessed by two-tailed

966 Student's t tests; error bars represent the standard deviation.

967

968 **Supplementary Figure 1. Immunohistological analysis of dermal mesenchymal cell**

969 **distribution in HSEs and human skin**

970 (a) Immunohistochemical analyses of HSEs and human skin samples to evaluate the

971 existence and distribution of dermal mesenchymal cell subpopulations. These samples

972 were stained with the papillary fibroblast markers CD39 and FAP, the reticular

973 fibroblast markers CD36 and CD90, and the pericyte markers NG2 and αSMA. The

974 dotted lines indicate the boundary between the epidermis and dermis. Scale bars, 100

975 μm.

976

977 **Supplementary Figure 2. scRNA-seq analysis of all in vitro samples.**

978 UMAP plot of scRNA-seq for in vitro human skin data, and distribution of all cells

979 under each of the three conditions (2D, 3D_ED, 3D_EDV).

980

981 **Supplementary Figure 3. Re-evaluation of in vivo samples through scRNA-seq**.

982 **a**, A Uniform Manifold Approximation and Projection (UMAP) plot presenting single-

983 cell transcriptomic data from whole human skin samples (n=5). Each point signifies a

984 single cell (n=), with coloration based on unsupervised clustering executed by Seurat. **b**,

985 Mean expression of genes forming the papillary and reticular gene signatures applied to

986 predict the dermal localization of fibroblasts within the four clusters. **c**, The top 10

987 significantly enriched Gene Ontology (GO) terms within each fibroblast subpopulation,

988 arranged by p-value. **d**, The UMAP plot features the average expression of previously

989 established cell type markers to distinguish cell populations. Red denotes maximum

990 gene expression, while blue represents minimal or non-existent expression of a specific

991 gene set in log-normalized UMI counts.

992

993 Table 1. **Primary and secondary antibodies.**

Antibodies	**Source**	**Cat#**	**Dilution ratio**
Primary			
Anti-Cytokeratin 5 antibody	Abcam	Ab52635	1/200
Anti-Cytokeratin 10 antibody	Abcam	Ab9026	1/200
Anti-Claudin 1 antibody	Abcam	ab211737	1/250
Filaggrin Monoclonal Antibody (FLG01)	Thermo Fisher Scientific	MA5-13440	1/50
Anti-Ki67 antibody	Abcam	ab156956	1/150
Anti-Collagen I antibody	Abcam	ab34710	1/200
Anti-Collagen IV antibody	Abcam	ab6311	1/250
Anti-CD31 antibody	Abcam	ab9498	1/1000
Anti-CD31 antibody	Abcam	ab28364	1/50
Anti-Von Willebrand Factor antibody	Abcam	ab778	1/50
anti-Collagen Type 1 (3/4 fragment), pAb	AdipoGen	AG-25T-0113	1/50
Anti-alpha smooth muscle Actin	Abcam	ab5694	1/100
Anti-NG2 antibody	Abcam	ab139406	1/250
Anti-Fibroblast activation protein, alpha antibody	Abcam	ab207178	1/250

Anti-CD36 antibody	Abcam	ab252923	1/250
Anti-CD39 antibody	Abcam	ab223842	1/1000
Anti-CD90 / Thy1 antibody	Abcam	ab92574	1/200
Anti-Vimentin antibody	Abcam	ab8978	1/500
Secondary			
Alexa Fluor® 594 donkey anti-rabbit IgG	Thermo Fisher Scientific	A21207	1/500
Alexa Fluor® 594 donkey anti-mouse IgG (H + L) antibody	Thermo Fisher Scientific	A21203	1/500
Alexa Fluor® 488 donkey anti-rabbit IgG (H + L)	Thermo Fisher Scientific	A21206	1/500
Alexa Fluor® 488 donkey anti-mouse IgG (H + L)	Thermo Fisher Scientific	A21202	1/500

The table shows the commercially available antibodies which were used for immunohistochemical analyses.

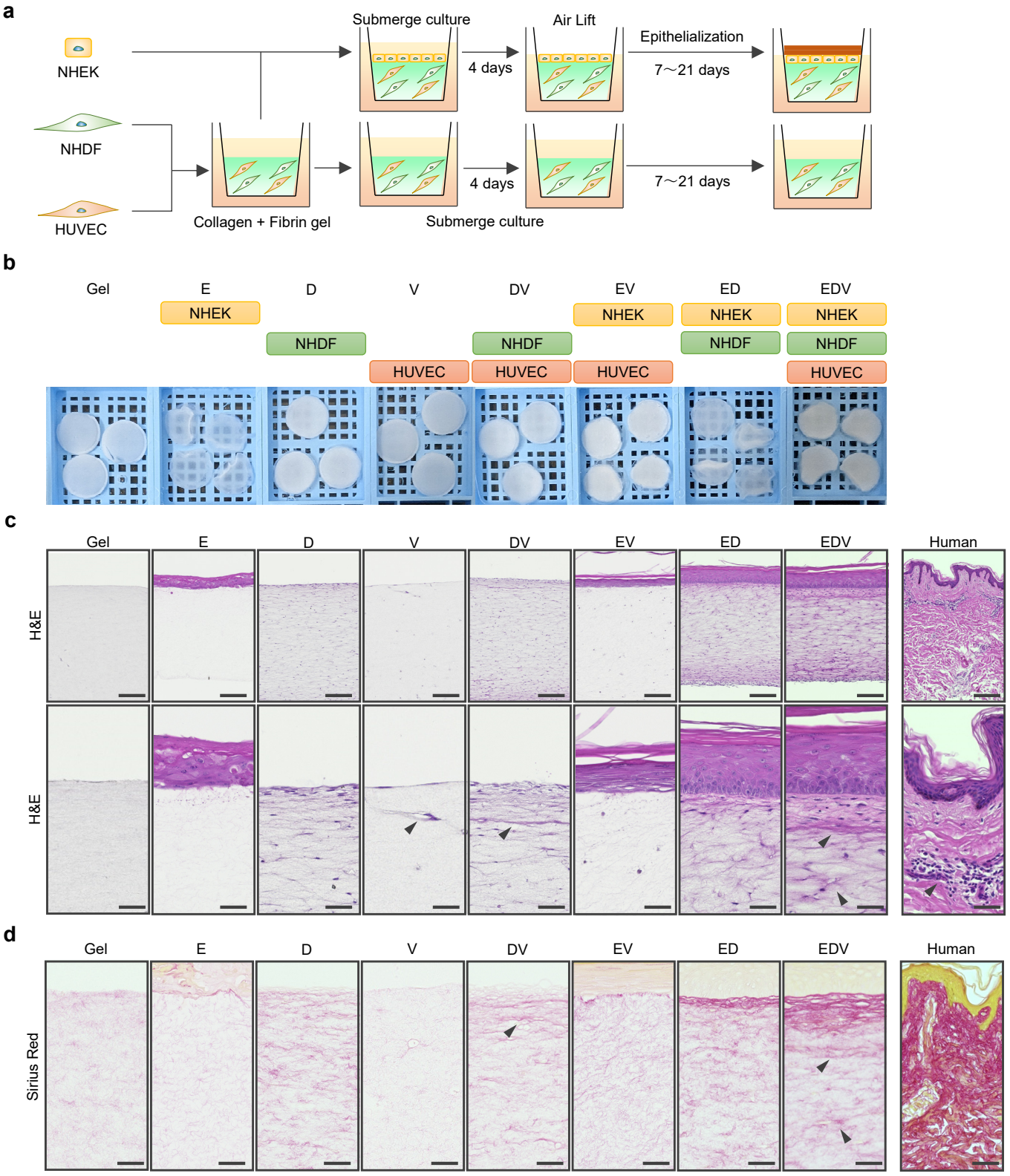

Figure 1 Tricellular communication regulates skin and vascular organization.
(a) Schematic representation of the construction method of HSEs. (b) Macroscopic images of the constructed HSEs. The abbreviations for the HSE and the constituent cell types are listed at the top of each image. Scale bars, 1 mm. (c) H&E staining images of human skin and the HSEs at low (upper columns; scale bars, 200 μm) and high (lower columns; scale bars, 50 μm) magnification. The arrowheads indicate the endothelial tube. (d) Sirius Red-stained images of human skin and the HSEs; scale bars, 50 μm.

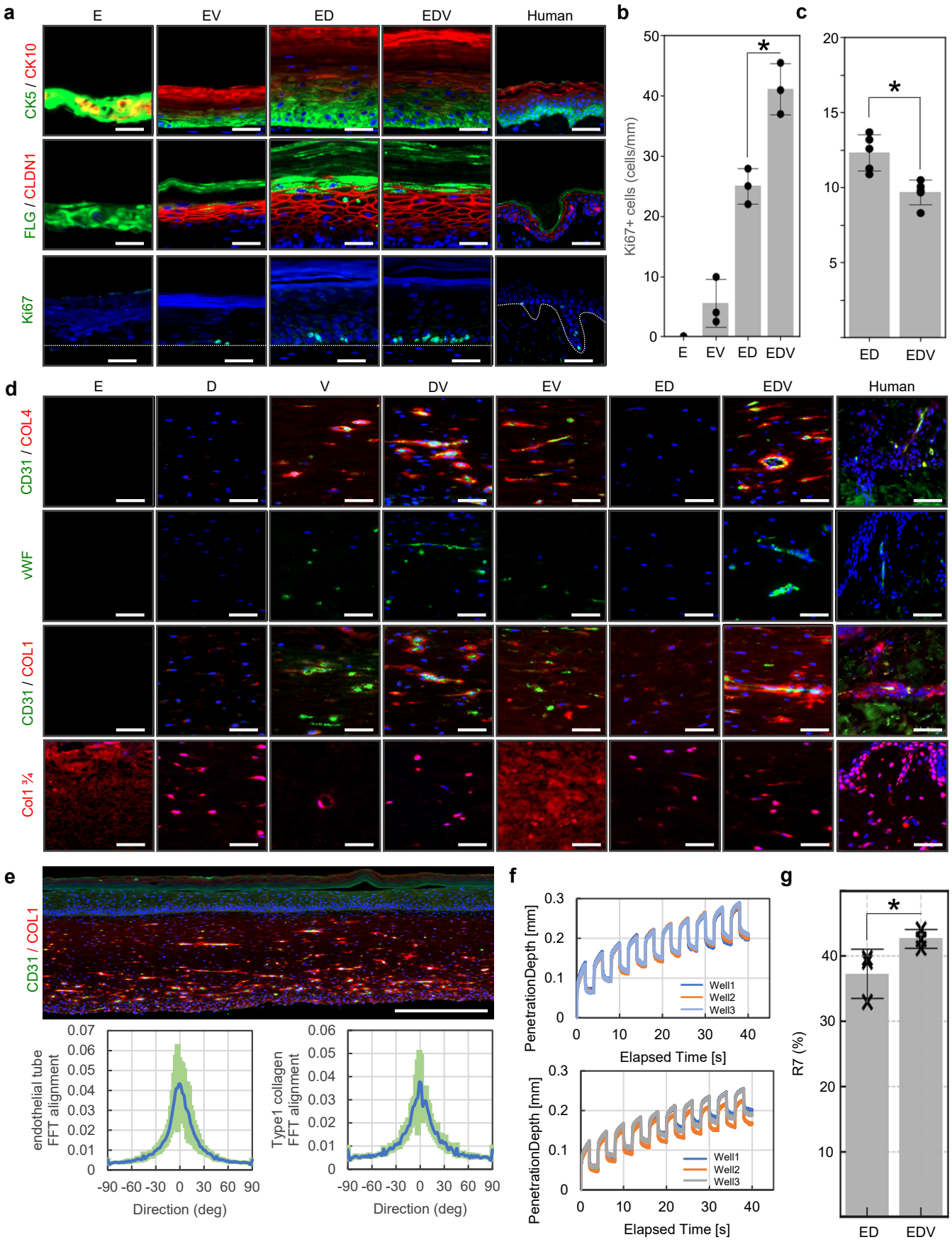

Figure 2 Tricellular communication enhances skin barrier function and elasticity by inducing self-organization.
(a) Immunohistochemical analyses of human skin and HSEs for evaluation of epithelialization. These samples were stained with CK5, CK10, CLDN1, FLG and Ki67 antibodies. The dotted lines indicate the boundary between the epidermis and dermis. Scale bars, 50 μm. (b) Analysis of the Ki67-positive basal keratinocyte ratio in HSEs. *P < 0.001, as assessed by Dunnett's test following two-way analysis of variance (ANOVA; P < 0.001). (c) TEWL analysis of the ED and EDV models. *P < 0.05 and, as assessed by two-tailed Student's t tests; error bars represent the standard deviation. (d) Immunohistochemical analyses of human skin and HSEs for evaluation of angiogenesis and dermal collagen synthesis. These samples were stained with CD31, COL4, vWF, COL1 and COL3/4 antibodies. (e) Macroscopic image of CD31 and COL1 distribution (upper column) and FFT analysis (lower columns) of the alignment of CD31-positive endothelial tubes and COL1-positive type 1 collagen fiber in the EDV model. Scale bars, 500 μm. (f) Skin deformation curves obtained from the ED model (upper panel) and EDV model. (g) R7 factor evaluation of the ED and EDV models. *P < 0.05 and, as assessed by two-tailed Student's t tests; error bars represent the standard deviation.

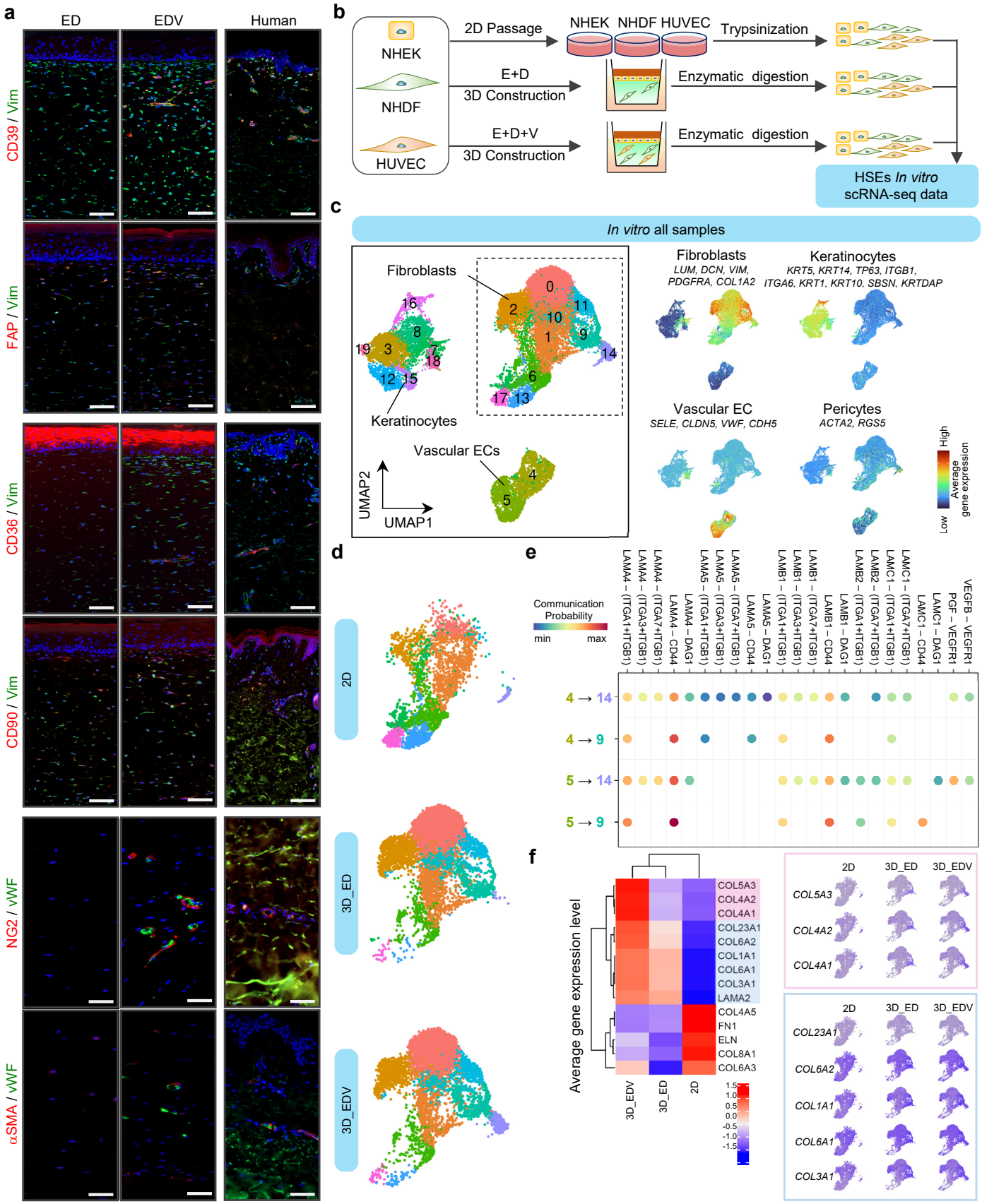

Figure 3. The three-dimensional culture environment and cell-to-cell communication replicate dermal mesenchymal cell heterogeneity *in vitro*.

(a) Immunohistochemical analyses of ED, EDV and human skin samples to evaluate the existence and distribution of dermal mesenchymal cell subpopulations. These samples were stained with the papillary fibroblast markers CD39 and FAP, the reticular fibroblast markers CD36 and CD90, and the pericyte markers NG2 and αSMA. The dotted lines indicate the boundary between the epidermis and dermis. Scale bars, 100 μm. (b) Illustration of the workflow for scRNA-seq data sampling and analysis. (c) UMAP plot of scRNA-seq data for in vitro HSEs; the average expression of four cell-type markers is projected onto the UMAP plot to identify cell populations. (d) Distribution of fibroblast and pericyte cells under each of the three conditions. (e) Cellular communication from vascular endothelial cells (ECs; Clusters #4 and #5) to pericytes in Cluster #14 and to fibroblasts in Cluster #9. (f) Heatmap showing the average expression levels of ECM-related genes across all fibroblasts under different conditions.

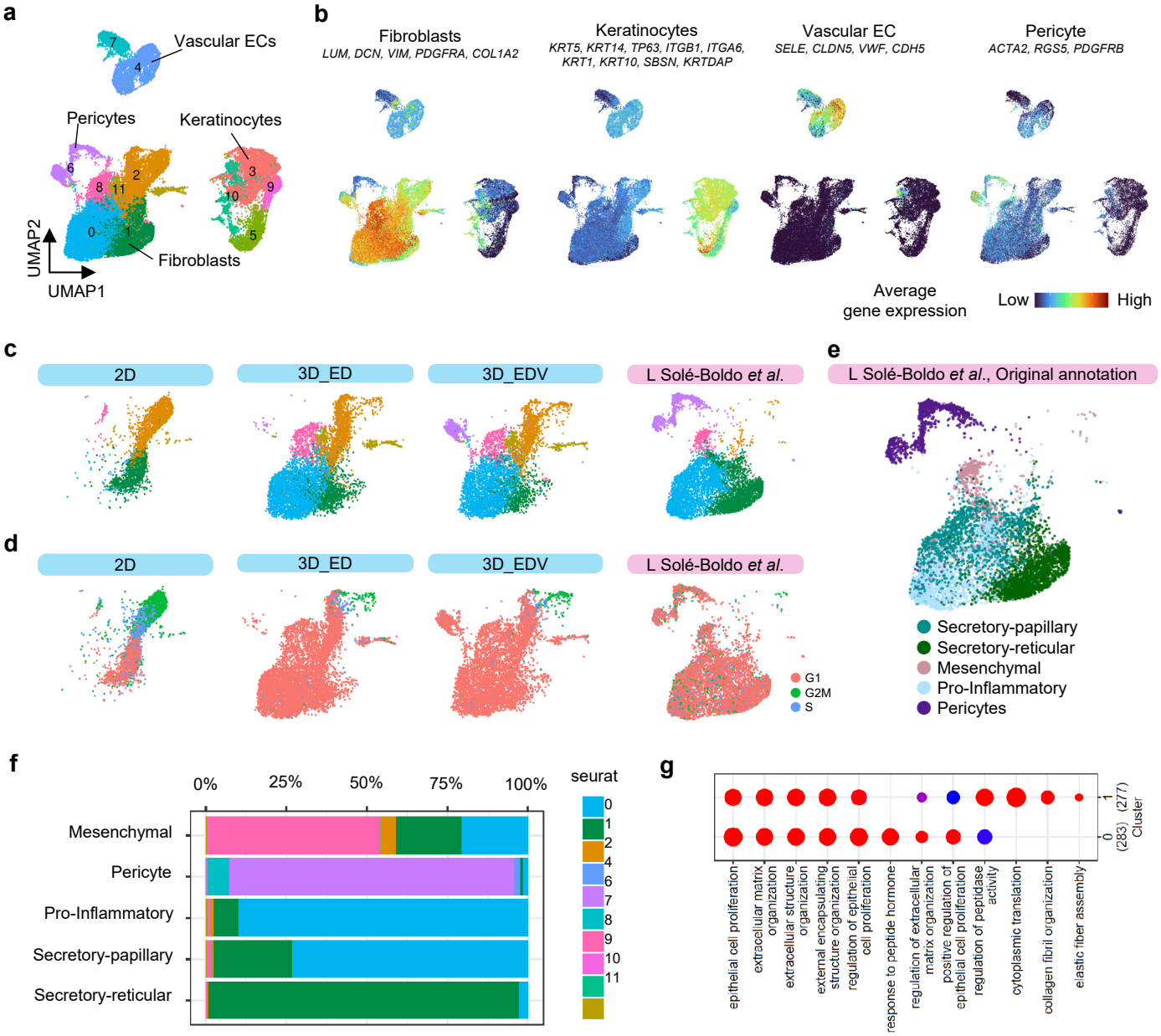

Figure 4 Analysis of the biological significance of fibroblast heterogeneity in HSEs through integrated analysis of human scRNA-seq data. (a) UMAP plot of scRNA-seq data for integrating in vitro artificial skin and in vivo skin data. (b) Average expression of established cell type markers was projected on the UMAP plot to identify cell populations. Red indicates maximum gene expression, whereas blue indicates low or no expression of a particular set of genes in log-normalized UMI counts. (c) UMAP plot integrating scRNA-seq data from *in vitro* HSEs and *in vivo* skin, showing the distribution of fibroblasts and pericytes across each of the three *in vitro* conditions and the *in vivo* condition. (d) Cell cycle status of fibroblasts under each condition. (e) UMAP plot showing the correspondence of the four fibroblast subpopulations and pericytes defined by L. Solé-Boldo *et al.* (f) Proportion of cells from each subpopulation as defined by L. Solé-Boldo *et al.* and their clustering into specific clusters, as shown in Fig. 4e. (g) Enriched Gene Ontology (GO) terms in clusters #0' and #1'.

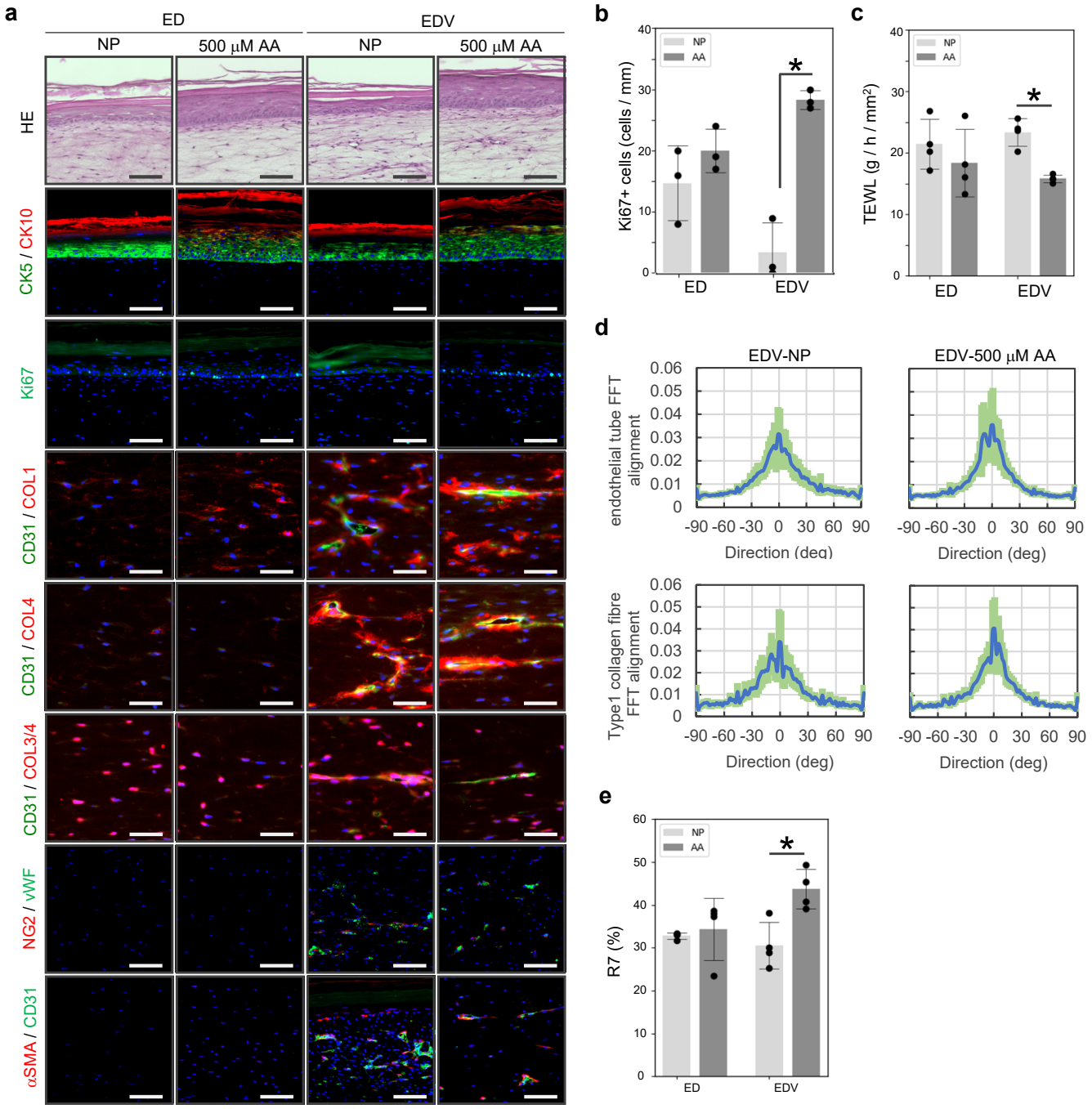

Figure 5 Nutrient-poor culture conditions in the HSEs induce a senescent phenotype, which is suppressed by ascorbic acid. Histological analysis of skin tissue organization induced by ascorbic acid supplementation in nutrient-poor cultured HSEs.These samples were stained with H&E, CK5, CK10, CLDN1, FLG and Ki67 antibodies. The dotted lines indicate the boundary between the epidermis and dermis. Scale bars, 50 µm. (b) Analysis of the Ki67-positive basal keratinocyte ratio in HSEs. *P < 0.001, as assessed by two-tailed Student's t tests; error bars represent the standard deviation.(c) TEWL analysis of the ED and EDV models. *P < 0.001, as assessed by two-tailed Student's t tests; error bars represent the standard deviation. (d) 2D-FFT analysis (lower columns) of the alignment of CD31-positive endothelial tubes and COL1-positive type 1 collagen fiber in the EDV model. (e) R7 factor evaluation of the ED and EDV models. *P < 0.01 and, as assessed by two-tailed Student's t tests; error bars represent the standard deviation.

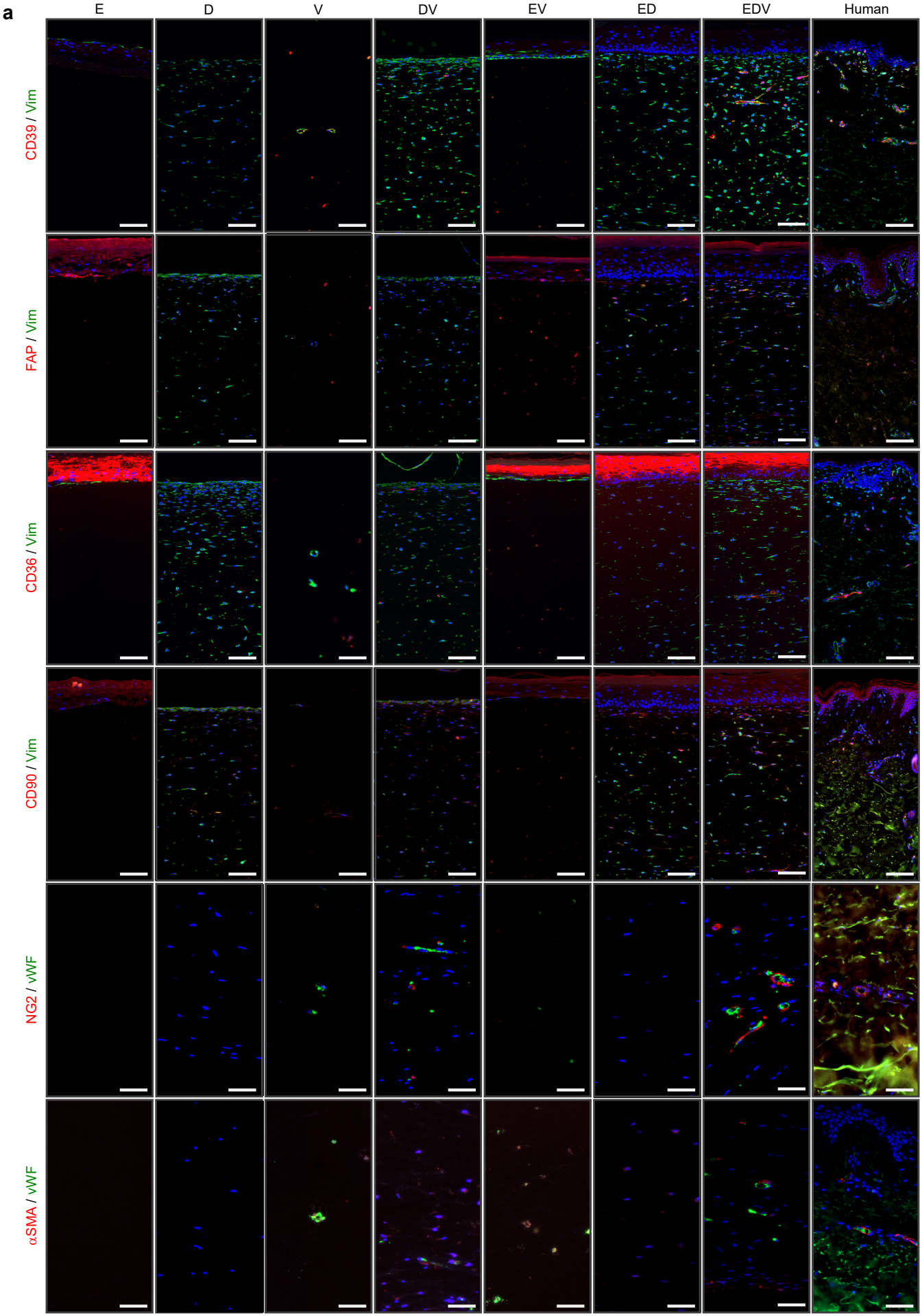

Supplementary Figure 1. Immunohistological analysis of dermal mesenchymal cell distribution in HSEs and human skin
(a) Immunohistochemical analyses of HSEs and human skin samples to evaluate the existence and distribution of dermal mesenchymal cell subpopulations. These samples were stained with the papillary fibroblast markers CD39 and FAP, the reticular fibroblast markers CD36 and CD90, and the pericyte markers NG2 and αSMA. The dotted lines indicate the boundary between the epidermis and dermis. Scale bars, 100 μm.

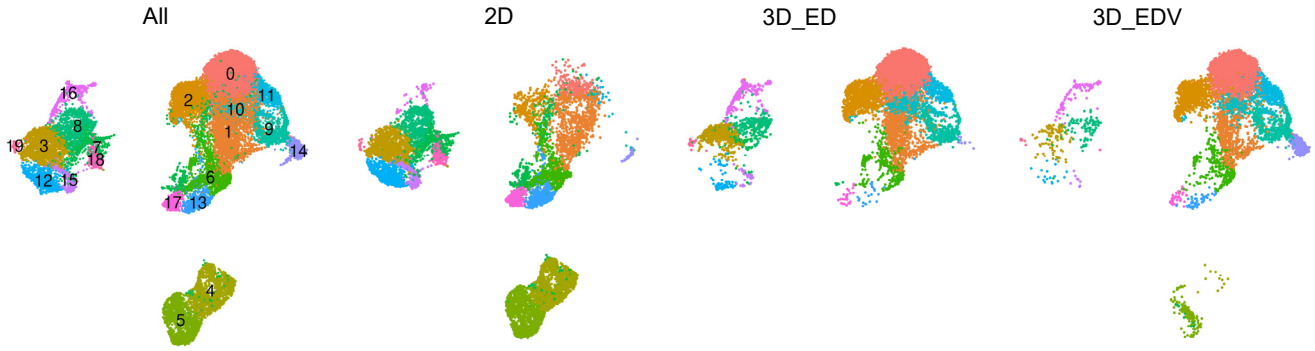

Supplementary Figure 2. scRNA-seq analysis of all in vitro samples.
UMAP plot of scRNA-seq for in vitro human skin data, and distribution of all cells under each of the three conditions (2D, 3D_ED, 3D_EDV).

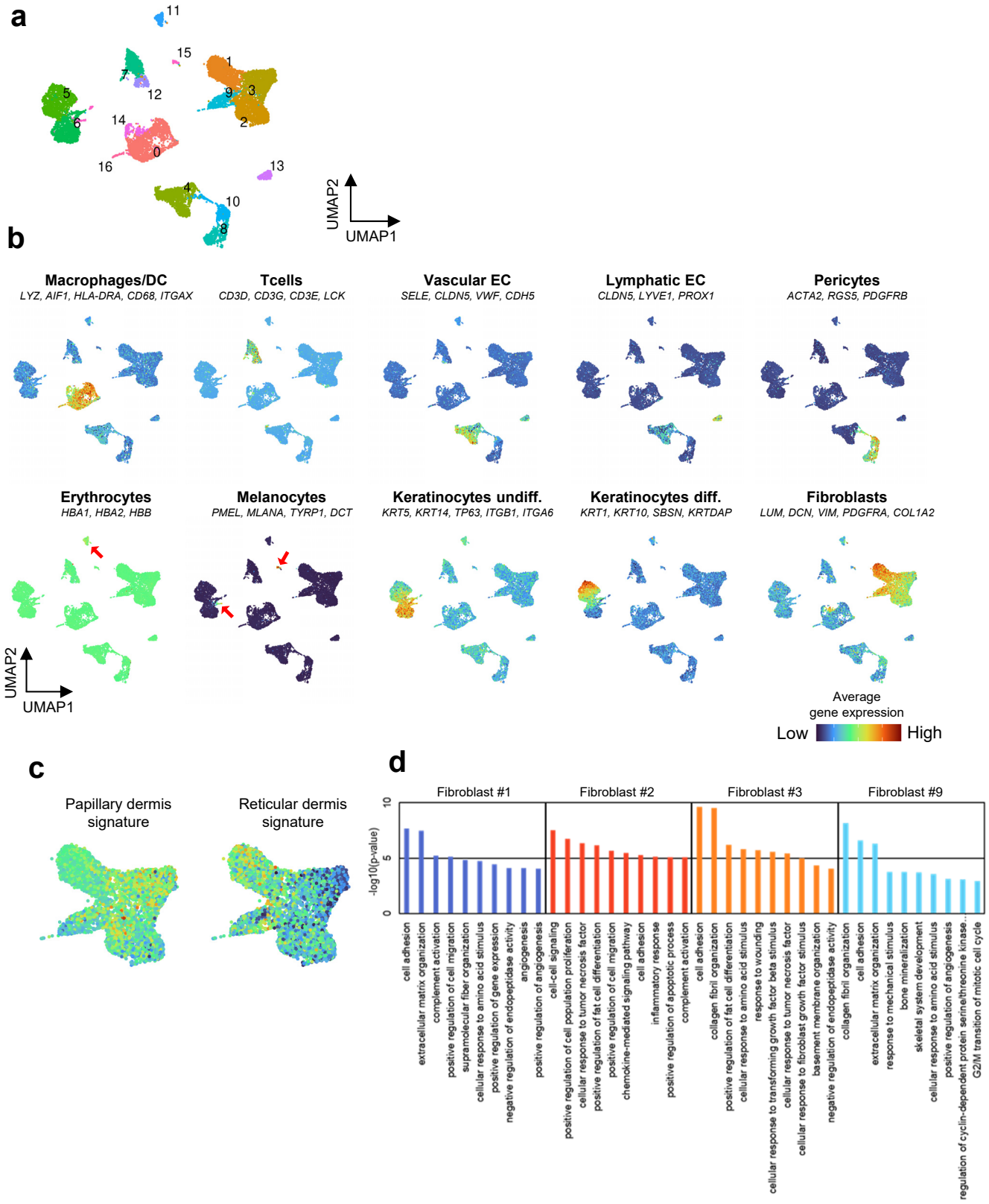

Supplementary Figure 3. Re-evaluation of in vivo samples through scRNA-seq.
a, A Uniform Manifold Approximation and Projection (UMAP) plot presenting single-cell transcriptomic data from whole human skin samples (n=5). Each point signifies a single cell (n=), with coloration based on unsupervised clustering executed by Seurat. **b**, Mean expression of genes forming the papillary and reticular gene signatures applied to predict the dermal localization of fibroblasts within the four clusters. **c**, The top 10 significantly enriched Gene Ontology (GO) terms within each fibroblast subpopulation, arranged by p-value. **d**, The UMAP plot features the average expression of previously established cell type markers to distinguish cell populations. Red denotes maximum gene expression, while blue represents minimal or non-existent expression of a specific gene set in log-normalized UMI counts.